*Supporting Information*

# Sn and Ge complexes with redox-active ligands as efficient interfacial membrane-like buffer layers for p-i-n perovskite solar cells

Azat F. Akbulatov[1], Anna Ya. Akyeva[2], Pavel G. Shangin[2], Nikita A. Emelianov[1], Irina V. Krylova[2], Mariya O. Markova[2,3], Liliya D. Labutskaya[2,4], Alexander V. Mumyatov[1], Egor I. Tuzharov[2], Dmitry A. Bunin[5], Lyubov A. Frolova[1], Mikhail P. Egorov[2], Mikhail A. Syroeshkin[2], and Pavel A. Troshin[1]

[1] Federal Research Center of Problems of Chemical Physics and Medicinal Chemistry, Russian Academy of Sciences, Academician Semenov ave. 1, Chernogolovka, Moscow Region, 142432 Russia

[2] N.D. Zelinsky Institute of Organic Chemistry, Russian Academy of Sciences, Moscow, 119991 Russia

[3] Dmitry Mendeleev University of Chemical Technology of Russia, Moscow, Russia

[4] Sechenov First Moscow State Medical University, Moscow, Russia

[5] A.N. Frumkin Institute of Physical Chemistry and Electrochemistry, Russian Academy of Sciences, Moscow, Russia

Correspondence: troshin2003@inbox.ru or troshin@icp.ac.ru

## Contents

**Table S1.** Crystal data, data collection and structure refinement details refinement for **1**.

| | | |
|---|---|---|
| Empirical formula | C30 H46 N2 O6 Sn2 | |
| Formula weight | 768.07 | |
| Temperature | 100.15 K | |
| Wavelength | 0.71073 Å | |
| Crystal system | Monoclinic | |
| Space group | $P2_1/c$ | |
| Unit cell dimensions | a = 8.34430(10) Å | α = 90°. |
| | b = 12.85750(10) Å | β = 101.7940(10)°. |
| | c = 14.5864(2) Å | γ = 90°. |
| Volume | 1531.89(3) $Å^3$ | |
| Z | 2 | |
| Density (calculated) | 1.665 $g/cm^3$ | |
| Absorption coefficient | 1.675 $mm^{-1}$ | |
| F(000) | 776 | |
| Crystal size | 0.12 x 0.04 x 0.03 $mm^3$ | |
| Theta range for data collection | 2.131 to 35.833°. | |
| Index ranges | -13<=h<=13, -20<=k<=19, -22<=l<=23 | |
| Reflections collected | 59080 | |
| Independent reflections | 6721 [R(int) = 0.0454] | |
| Observed reflections | 5974 | |
| Completeness to $\theta_{full}$ = 25.242° | 1.000 | |
| Max. and min. transmission | 1.00000 and 0.55356 | |
| Data / restraints / parameters | 6721 / 4 / 201 | |
| Goodness-of-fit on $F^2$ | 1.038 | |
| Final R indices [I>2σ(I)] | R1 = 0.0234, wR2 = 0.0547 | |
| R indices (all data) | R1 = 0.0293, wR2 = 0.0575 | |
| Largest diff. peak and hole | 1.509 and -0.991 $e.Å^{-3}$ | |

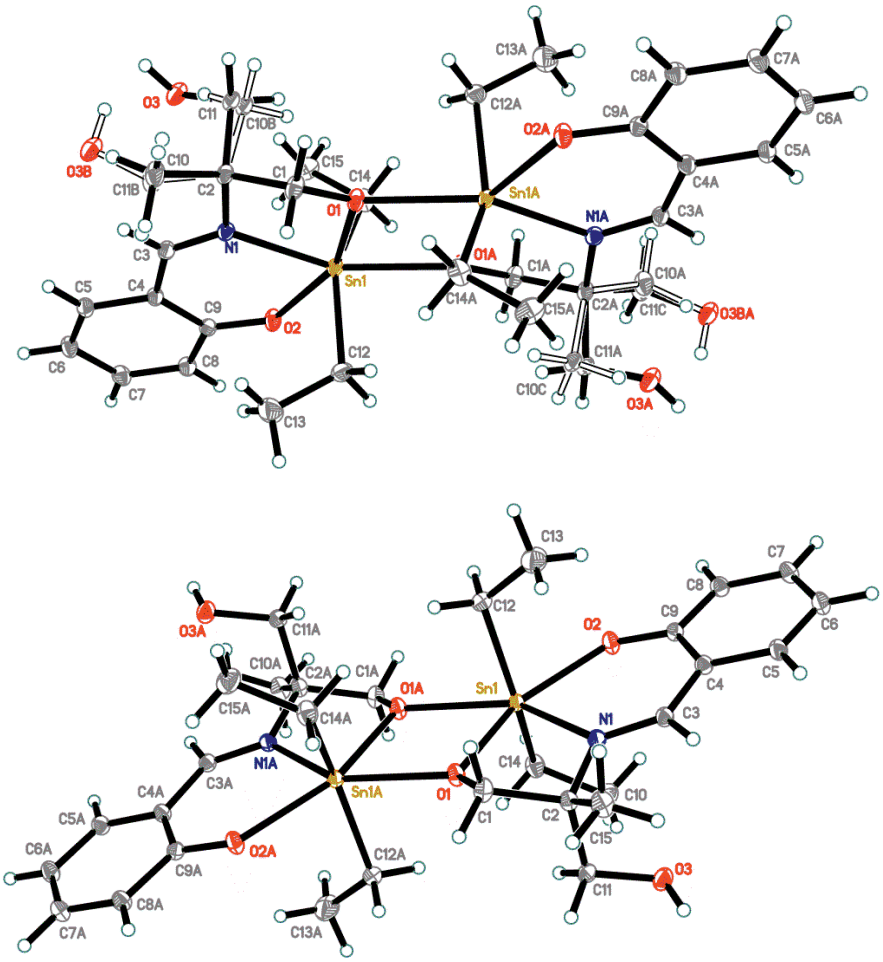


**Figure S1.** The molecular structure of **1** (p = 50%). A minor component of the OH disorder is shown in open solid lines; the disorder ratio is 0.909(3):0.091(3) (top). The disorder is omitted (bottom).

**Table S2**. Selected bond lengths [Å] for **1.**

| | | | | | |
|---|---|---|---|---|---|
| Sn(1)-O(1) | 2.0992(10) | N(1)-C(3) | 1.2942(16) | O(3A)-C(11A) | 1.412(3) |
| Sn(1)-O(1)#1 | 2.4090(10) | C(1)-C(2) | 1.5358(19) | C(11A)-C(2) | 1.545(2) |
| Sn(1)-O(2) | 2.2658(10) | C(4)-C(3) | 1.4431(18) | C(10A)-C(2) | 1.528(2) |
| Sn(1)-N(1) | 2.2369(11) | C(4)-C(9) | 1.4242(19) | O(3B)-C(11B) | 1.412(4) |
| Sn(1)-C(12) | 2.1298(14) | C(4)-C(5) | 1.4146(18) | C(11B)-C(2) | 1.545(4) |
| Sn(1)-C(14) | 2.1365(14) | C(6)-C(5) | 1.3781(19) | C(10B)-C(2) | 1.528(4) |
| O(2)-C(9) | 1.3085(16) | C(6)-C(7) | 1.400(2) | C(12)-C(13) | 1.523(2) |
| O(1)-C(1) | 1.4078(16) | C(8)-C(7) | 1.3791(19) | C(14)-C(15) | 1.528(2) |
| N(1)-C(2) | 1.4850(17) | C(8)-C(9) | 1.4175(18) | | |

Symmetry transformations used to generate equivalent atoms: #1 -x+1,-y,-z+1

**Table S3**. Selected bond angles [°] for **1.**

| | | | |
|---|---|---|---|
| O(2)-Sn(1)-O(1)#1 | 133.29(3) | C(14)-Sn(1)-O(2) | 84.83(5) |
| O(1)-Sn(1)-O(2) | 157.64(4) | C(14)-Sn(1)-O(1)#1 | 83.85(5) |
| O(1)-Sn(1)-O(1)#1 | 69.07(4) | C(14)-Sn(1)-N(1) | 105.92(5) |
| O(1)-Sn(1)-N(1) | 76.33(4) | C(9)-O(2)-Sn(1) | 132.51(8) |
| O(1)-Sn(1)-C(12) | 101.62(5) | Sn(1)-O(1)-Sn(1)#1 | 110.93(4) |
| O(1)-Sn(1)-C(14) | 100.17(5) | C(1)-O(1)-Sn(1) | 115.20(8) |
| N(1)-Sn(1)-O(2) | 81.34(4) | C(1)-O(1)-Sn(1)#1 | 128.70(8) |
| N(1)-Sn(1)-O(1)#1 | 145.23(4) | C(3)-N(1)-Sn(1) | 128.28(9) |
| C(12)-Sn(1)-O(2) | 84.13(5) | C(2)-N(1)-Sn(1) | 113.04(8) |
| C(12)-Sn(1)-O(1)#1 | 81.73(5) | C(13)-C(12)-Sn(1) | 115.66(10) |
| C(12)-Sn(1)-N(1) | 102.52(5) | C(15)-C(14)-Sn(1) | 115.35(10) |
| C(12)-Sn(1)-C(14) | 147.46(6) | | |

Symmetry transformations used to generate equivalent atoms: #1 -x+1,-y,-z+1

**Table S4**. Hydrogen bonds for **1** [Å and °].

| D-H...A | d(D-H) | d(H...A) | d(D...A) | <(DHA) |
|---|---|---|---|---|
| O(3B)-H(3B)...O(2)#2 | 0.83 | 2.35 | 3.036(12) | 140.0 |
| O(3A)-H(3A)...O(2)#2 | 0.83(3) | 1.97(3) | 2.7712(16) | 161(3) |

Symmetry transformations used to generate equivalent atoms: #1 -x+1, -y, -z+1 ; #2 x, -y+1/2, z+1/2

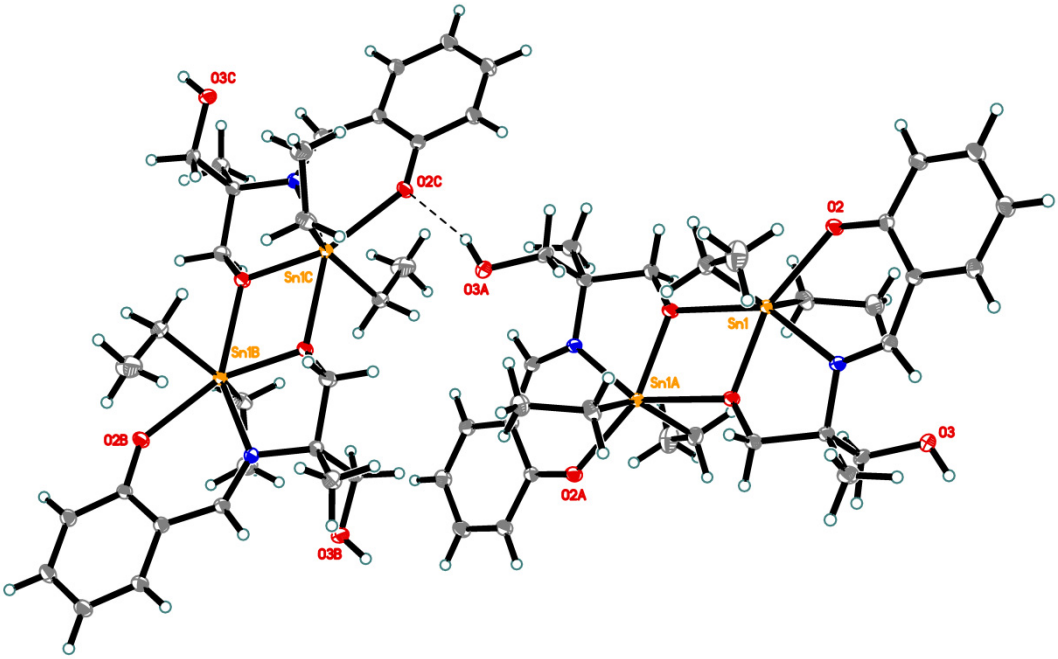


**Figure S2.** Hydrogen bonding in **1**. The OH disorder is omitted.

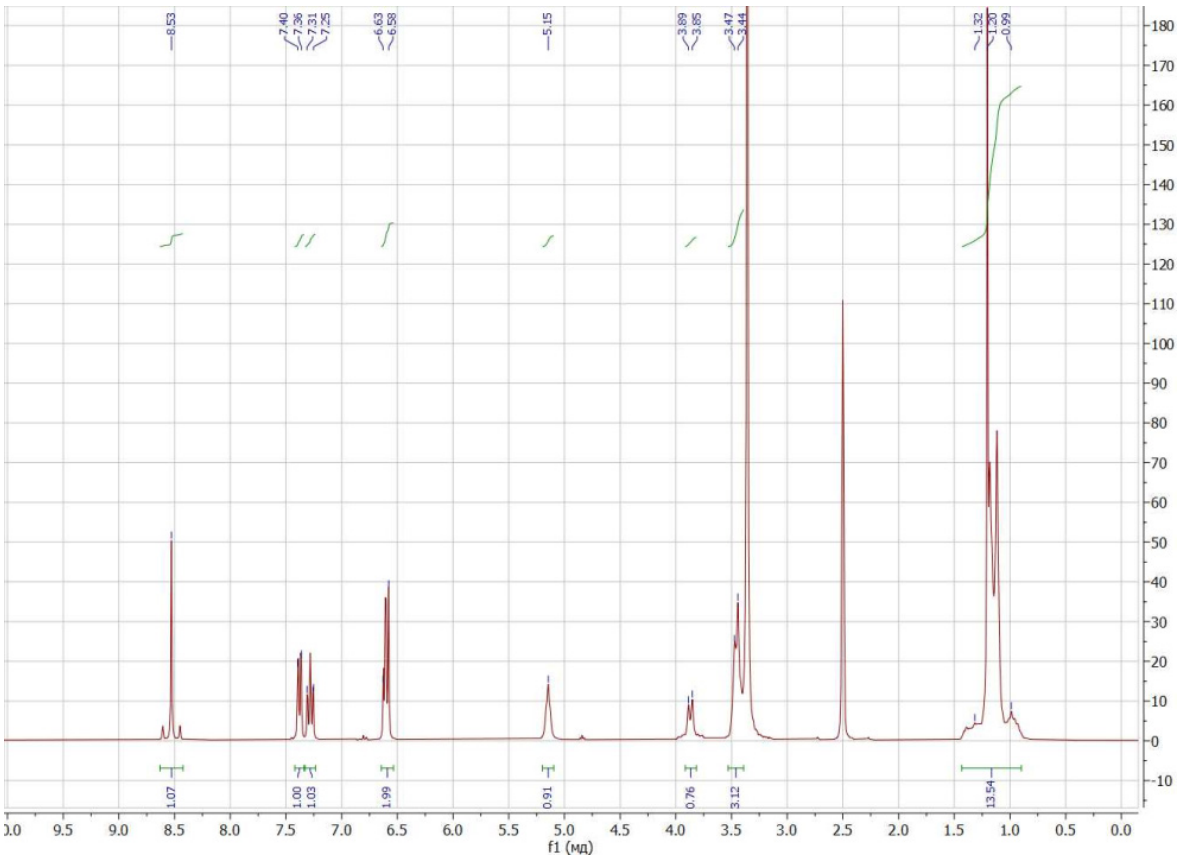


**Figure S3.** $^{1}$H spectrum of compound **1**.

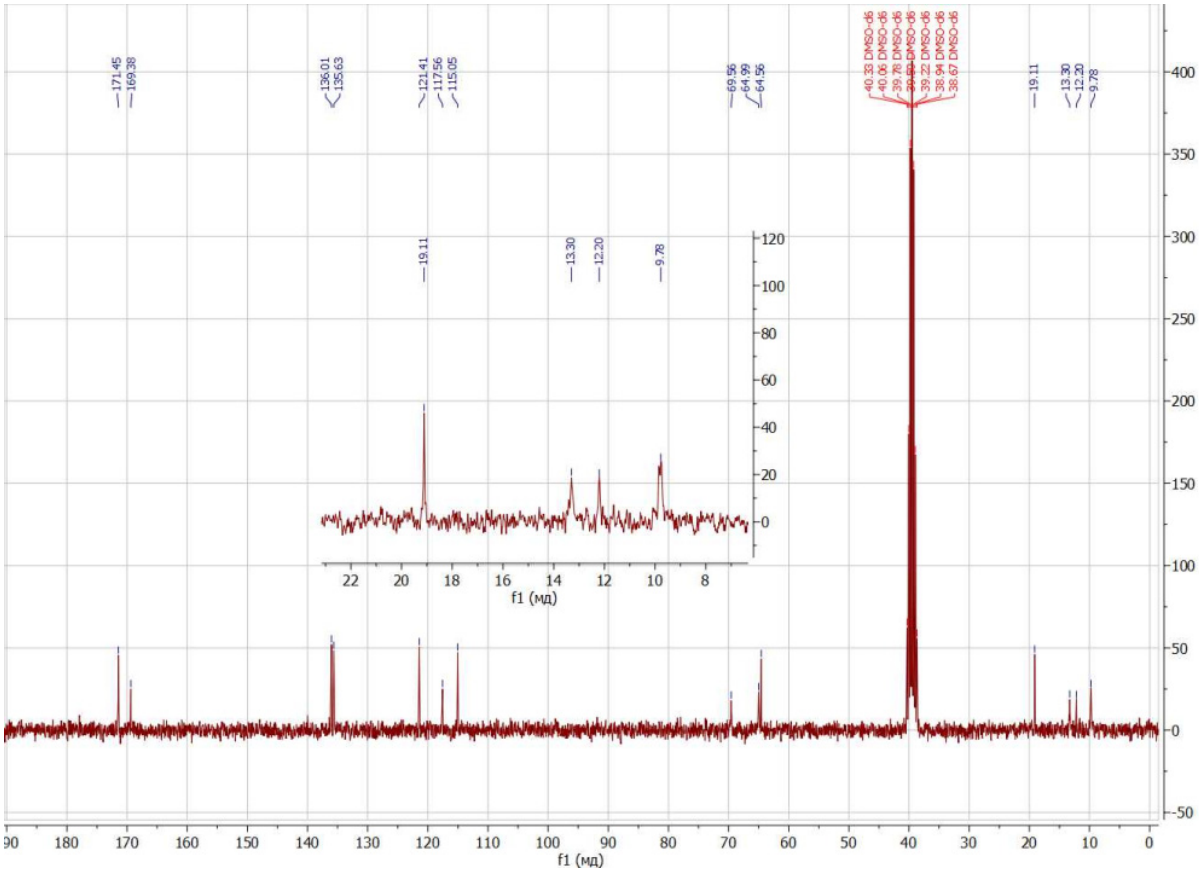


**Figure S4.** $^{13}$C NMR spectrum of compound **1**.

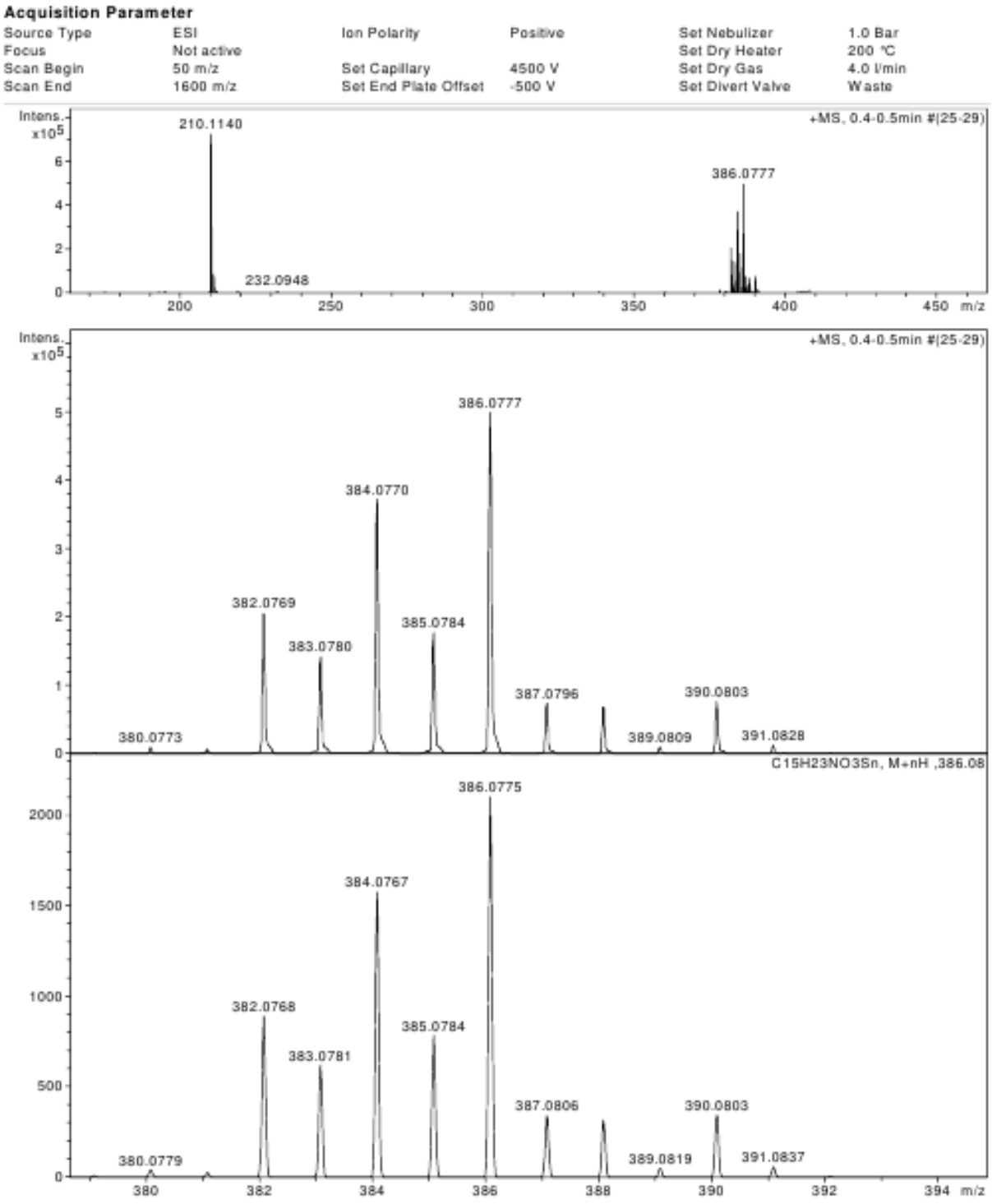


**Figure S5.** HRMS spectra of compound **1.**

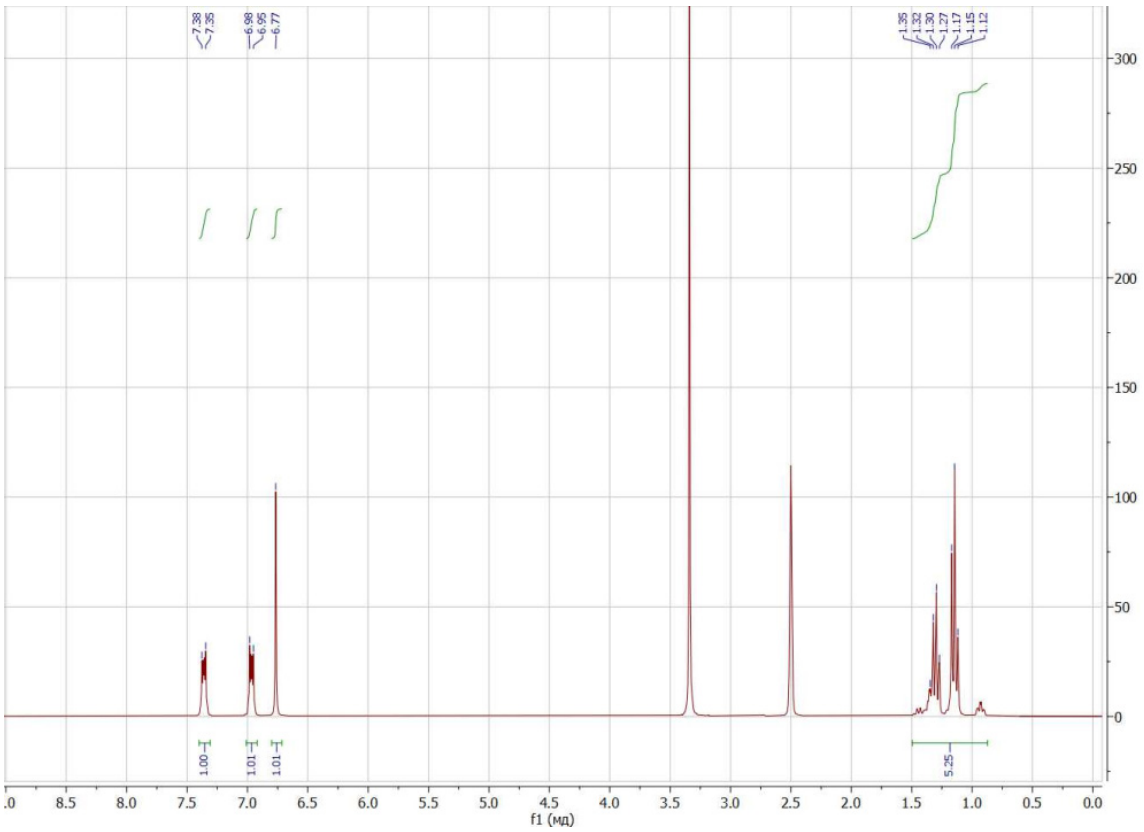


**Figure S6.** $^{1}$H NMR spectrum of compound **2**.

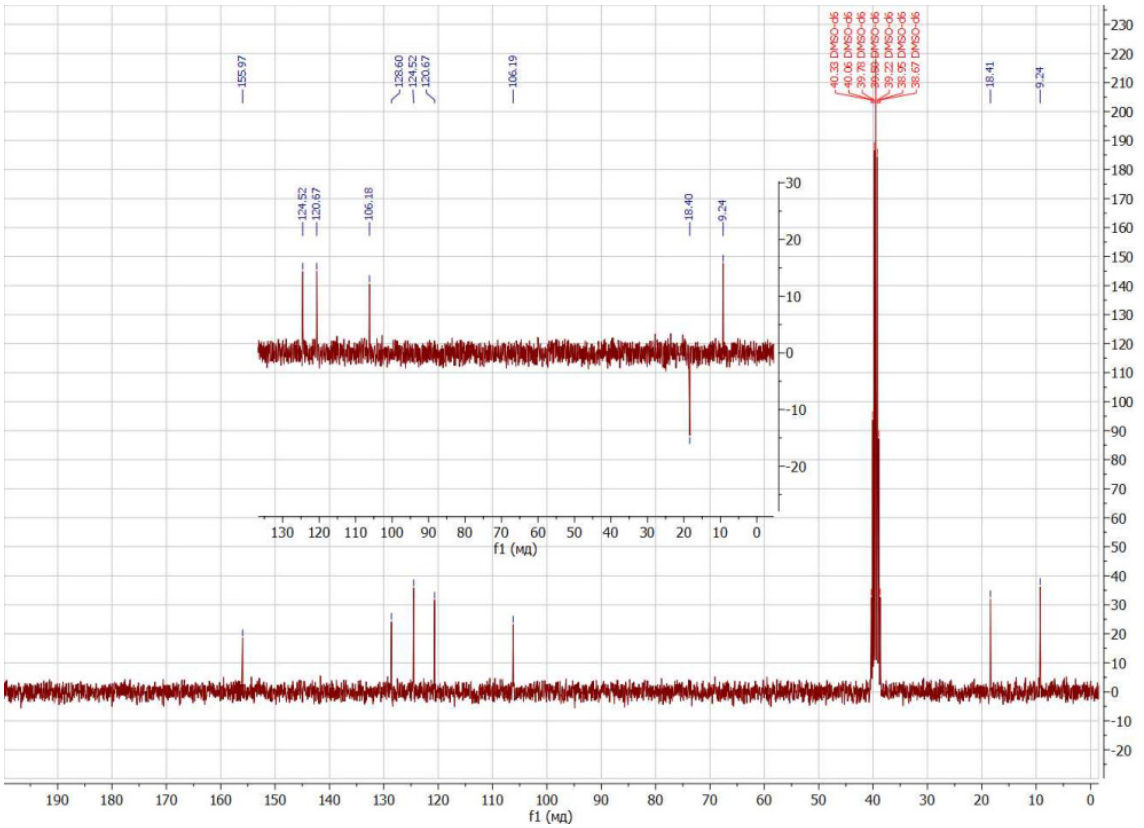


**Figure S7.** $^{13}$C NMR spectrum of compound **2**.

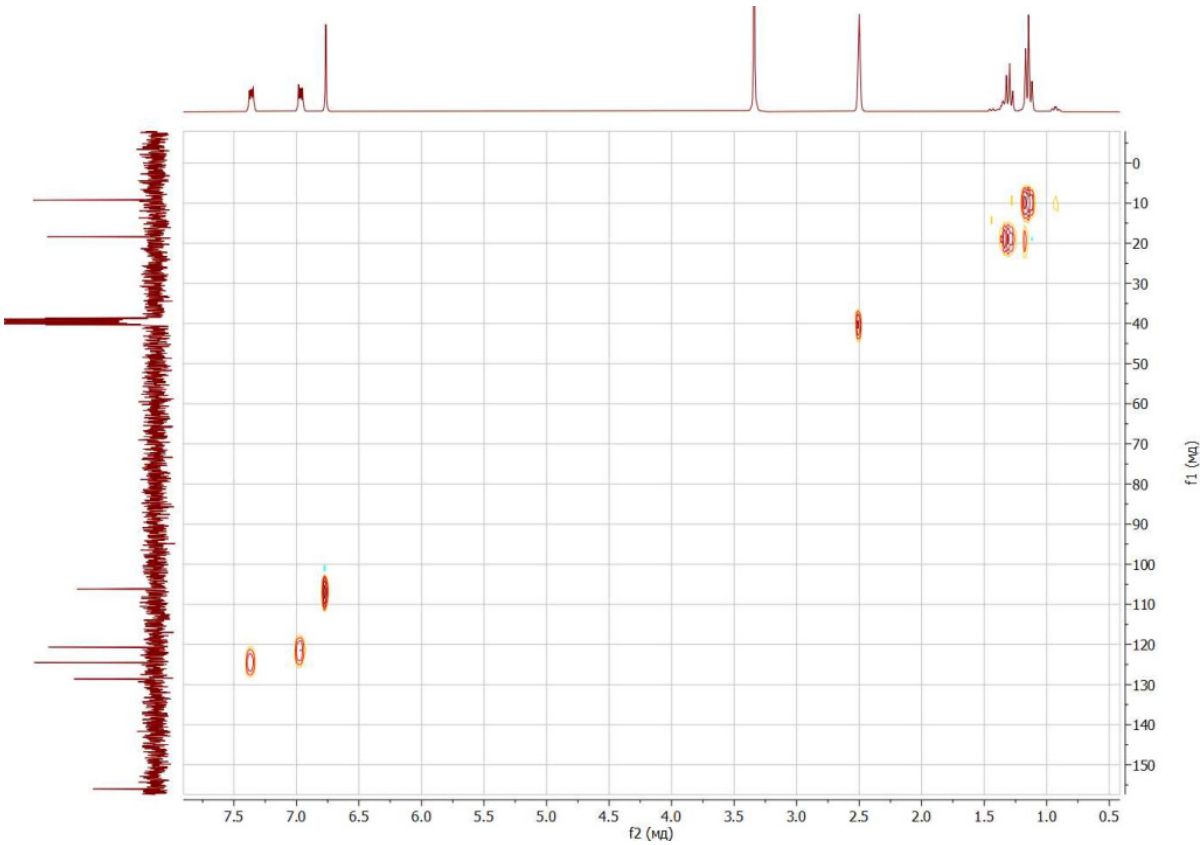


**Figure S8.** HSQC NMR spectrum of compound **2**.

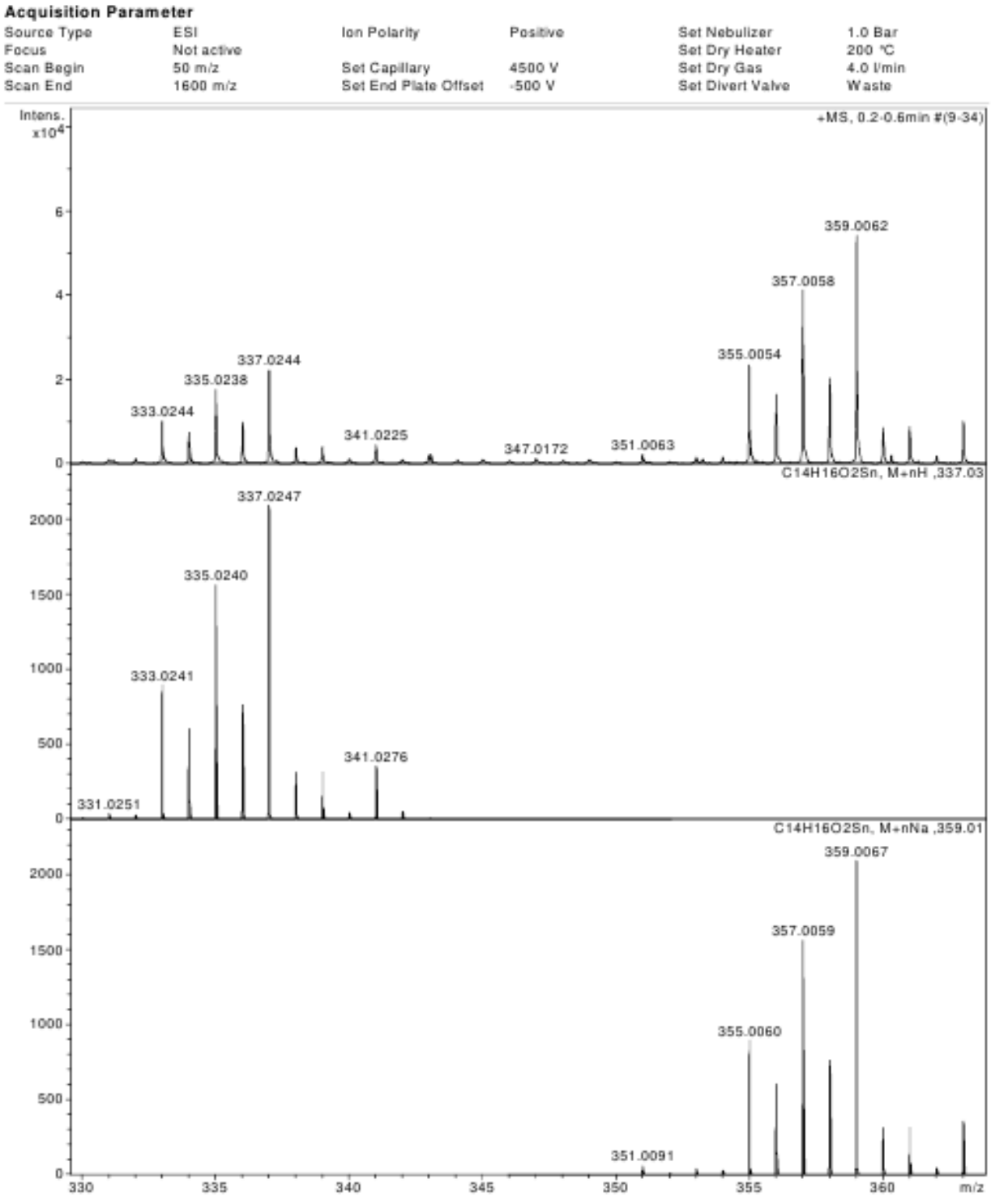


**Figure S9.** HRMS spectra of **2**.

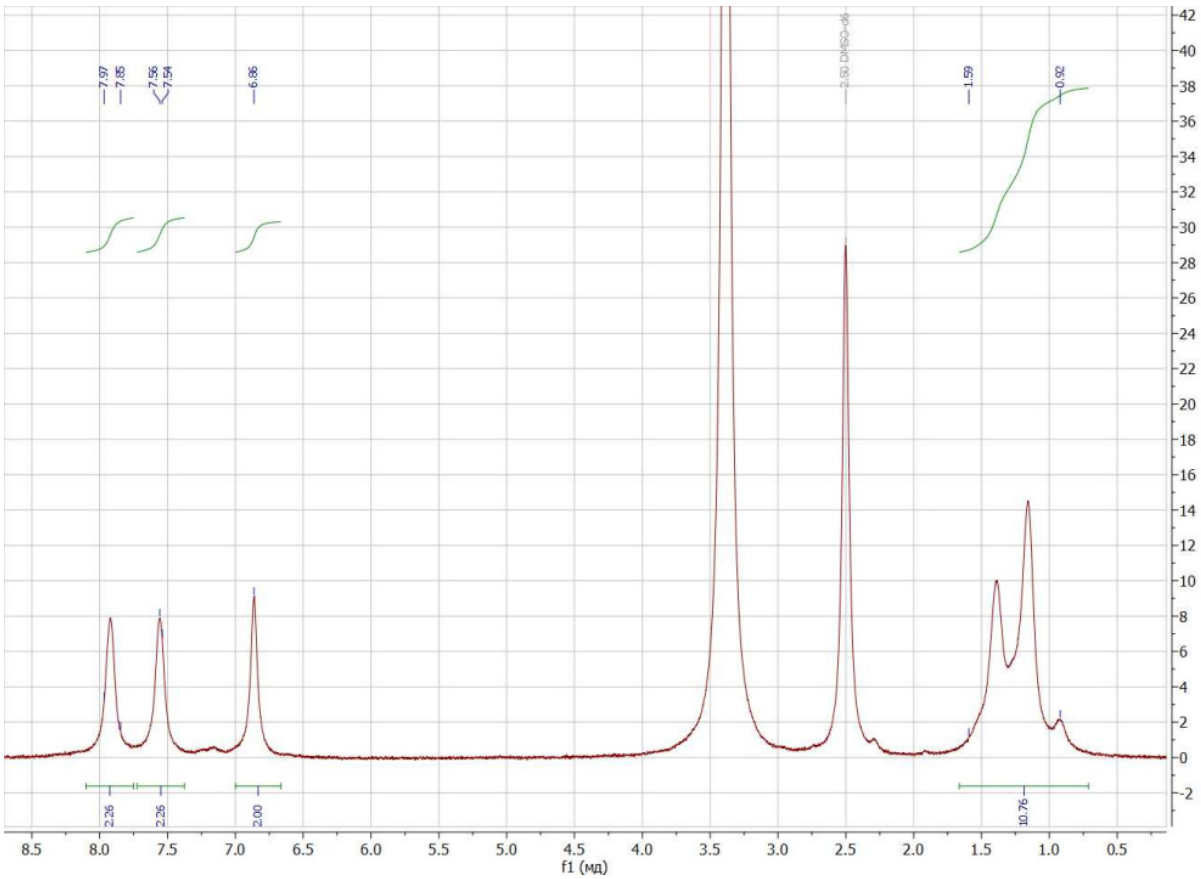


**Figure S10.** $^{1}$H NMR spectrum of compound **3**.

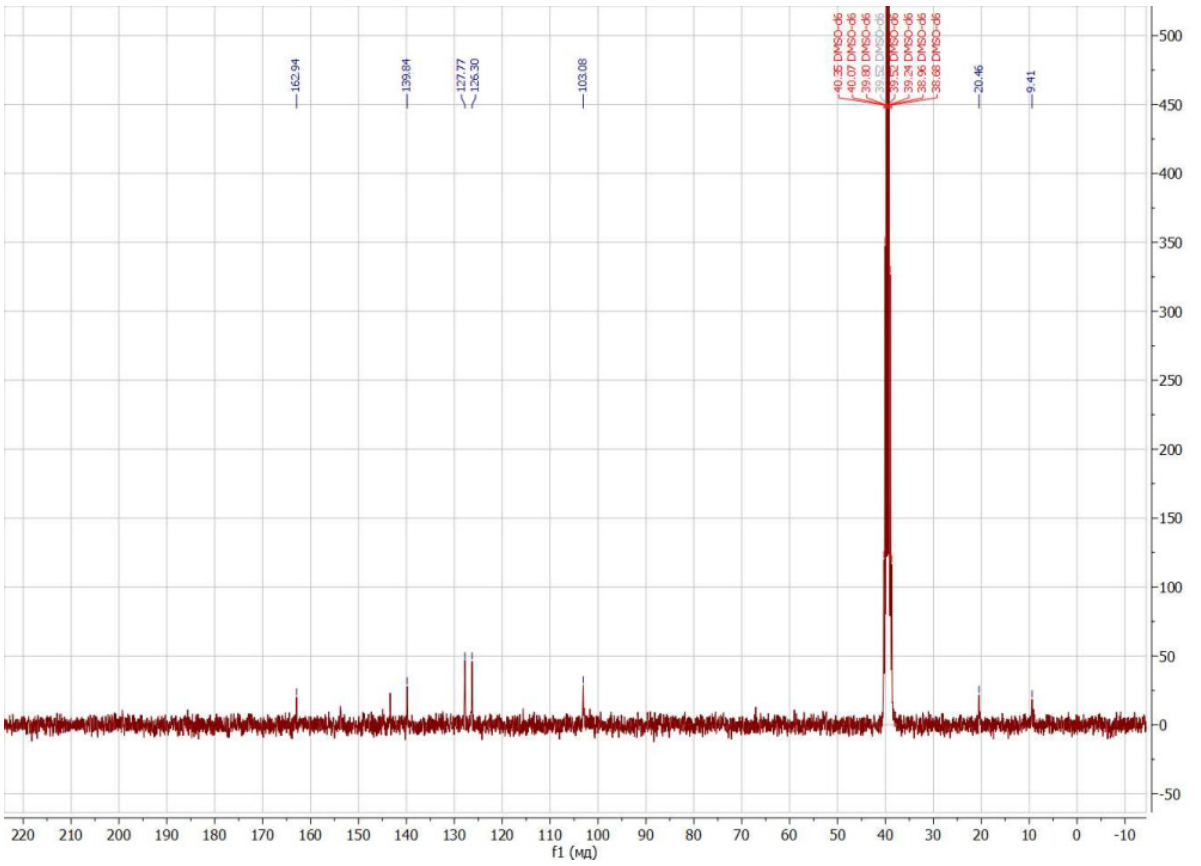


**Figure S11.** $^{13}$C NMR spectrum of compound **3**.

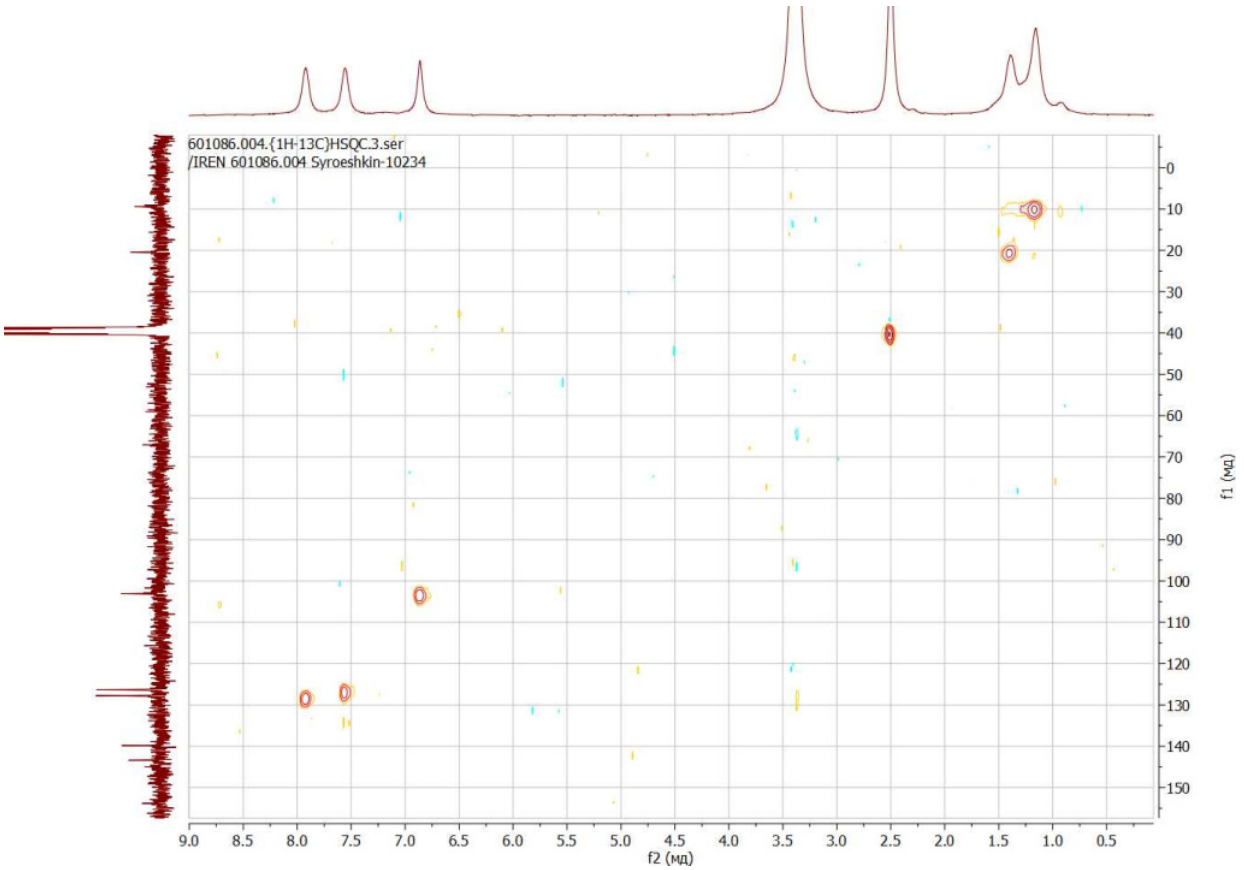


**Figure S12.** HSQC NMR spectrum of compound **3**.

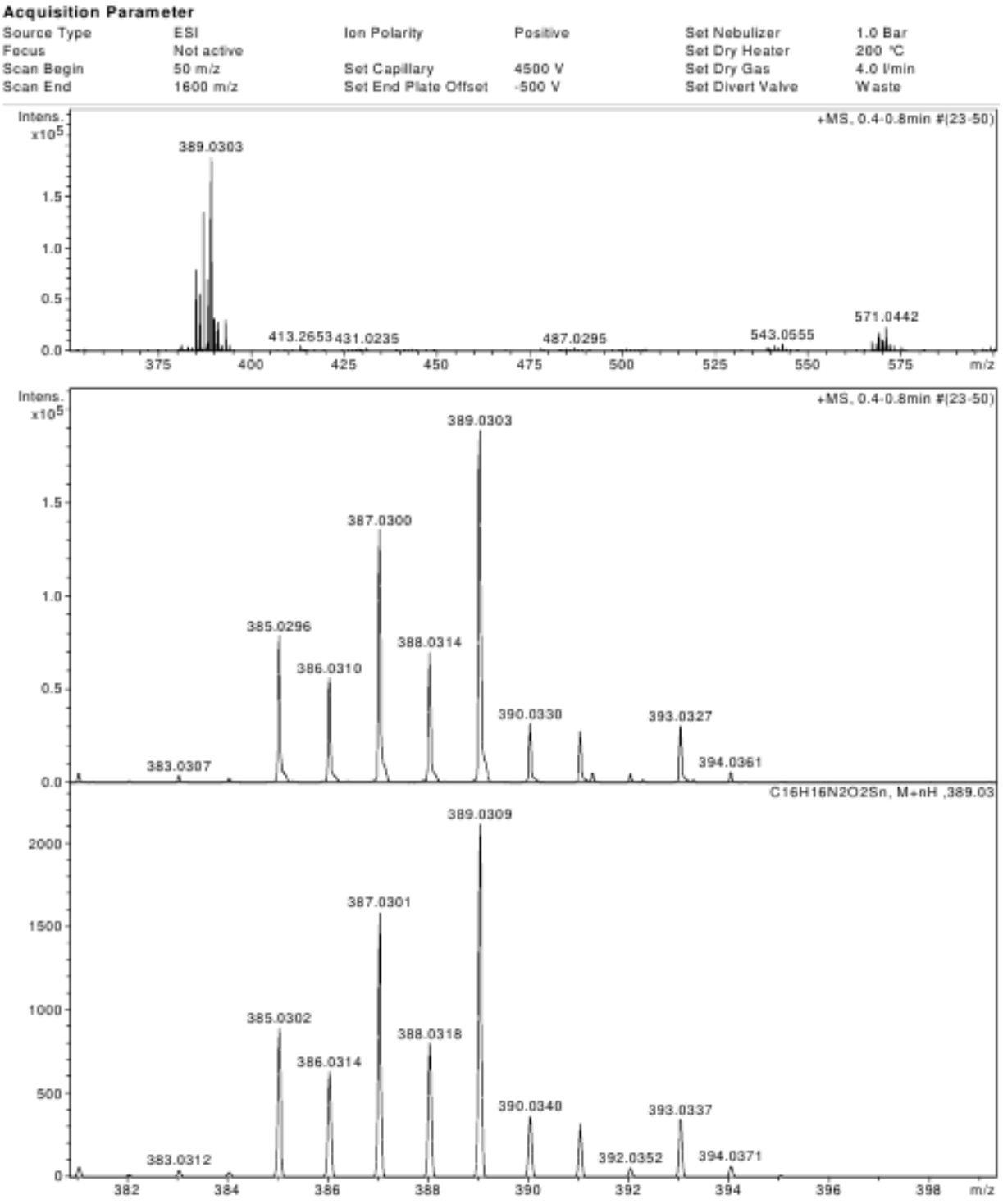


**Figure S13.** HRMS spectra of **3**.

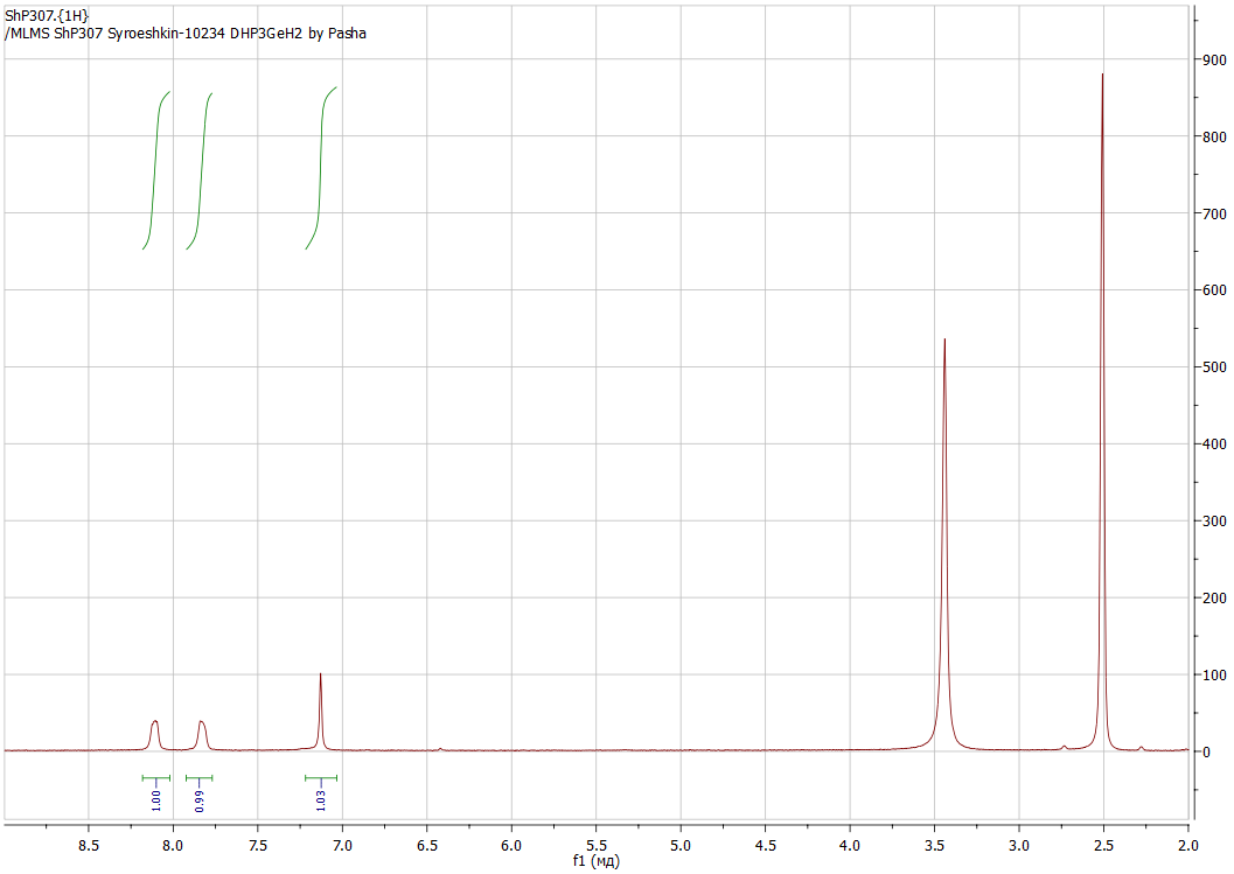


**Figure S14.** $^{1}$H NMR spectrum of compound **4**.

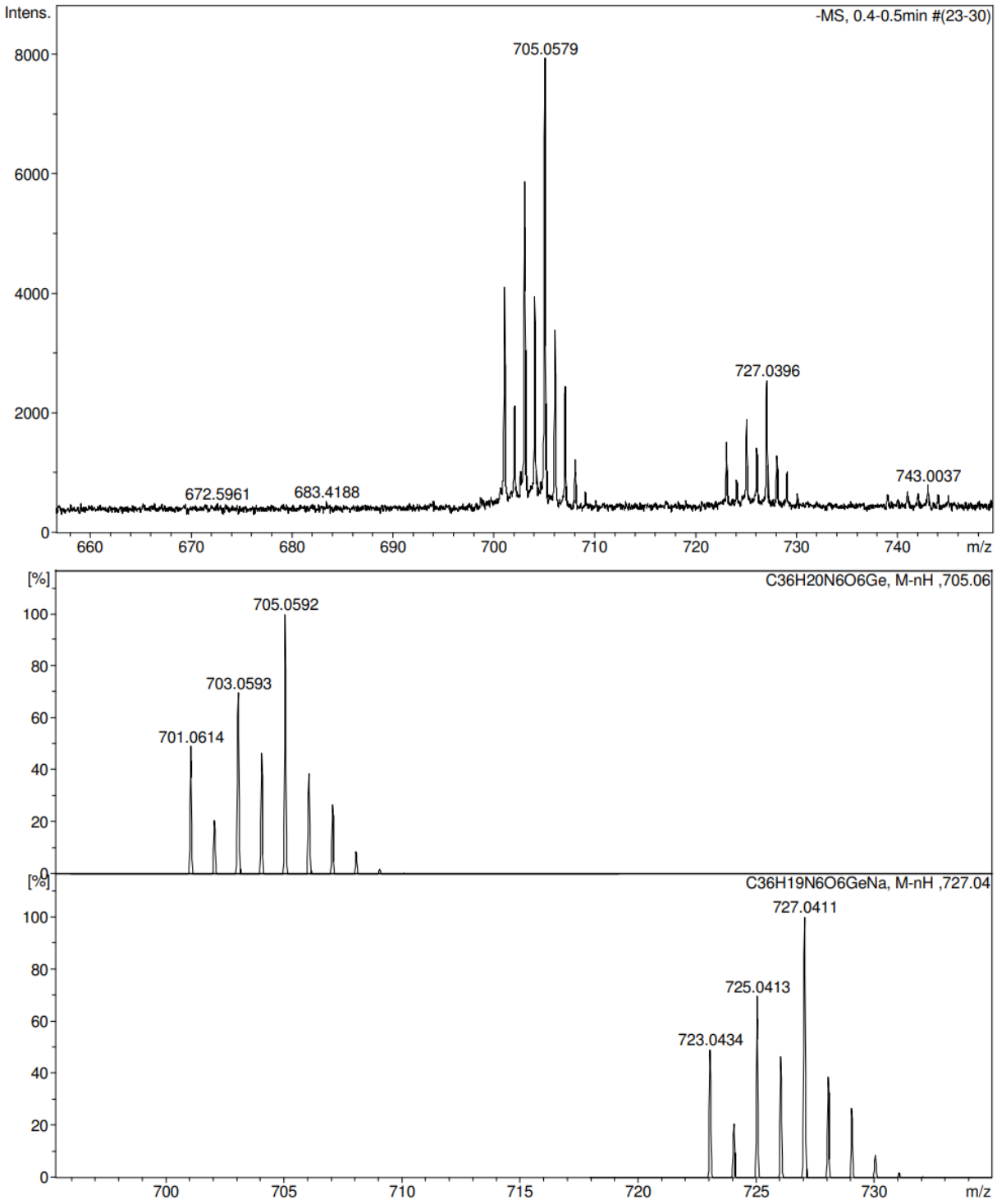


**Figure S15.** HRMS spectrum of **4**.

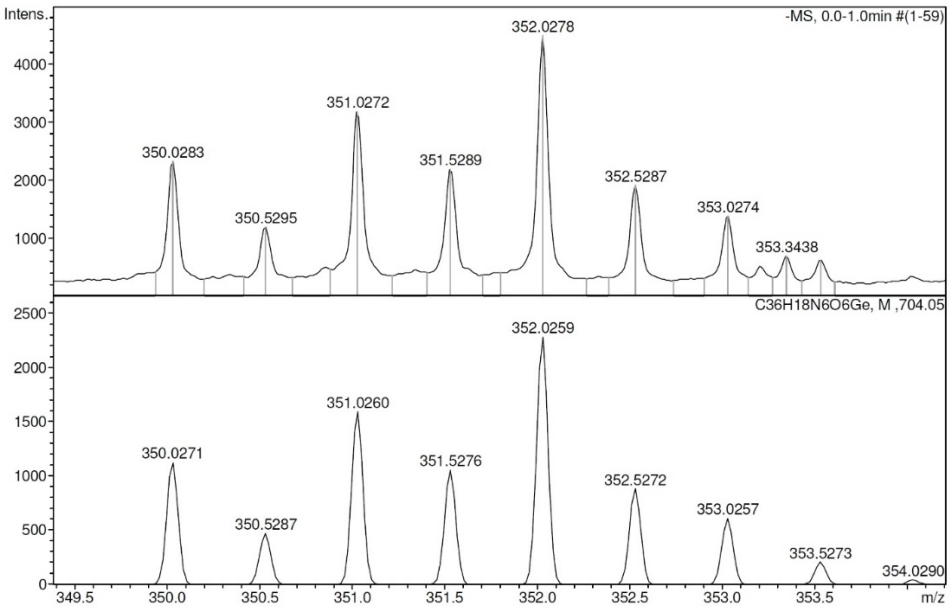


**Figure S16.** ESI-HRMS spectra (negative ion mode, MeOH) of the germanium dianion (*z* = 2) of **5**.

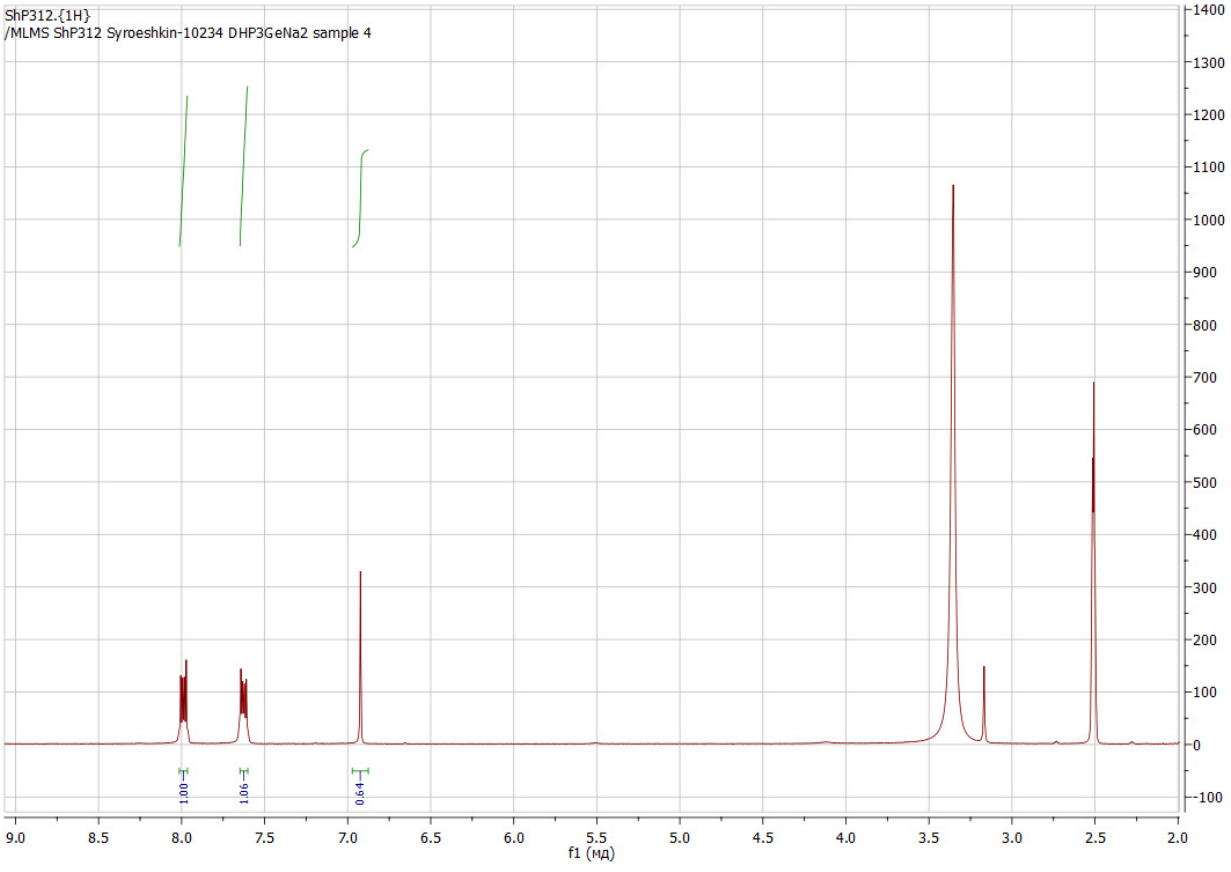


**Figure S17.** $^{1}$H NMR spectrum of compound **5**.

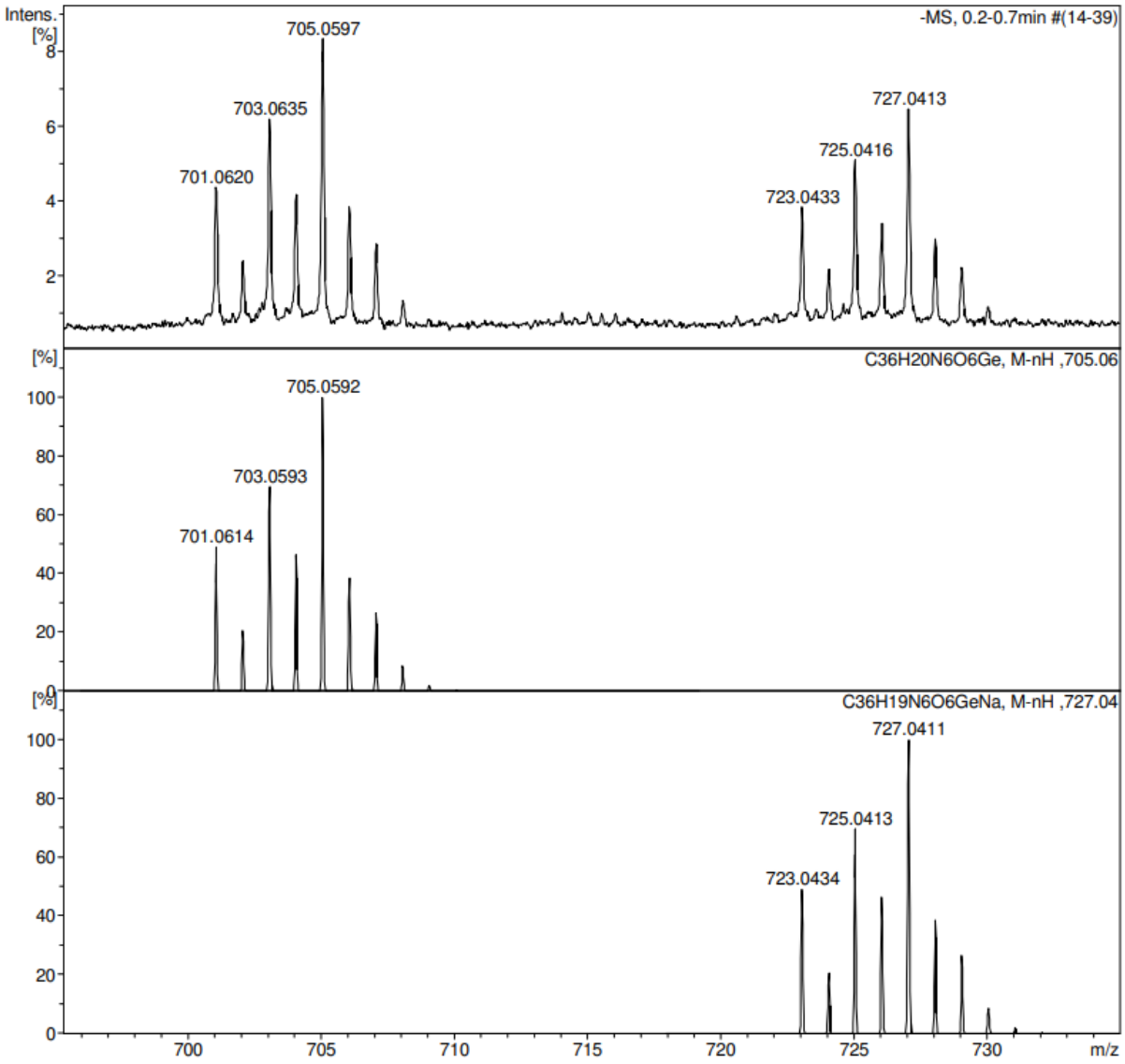


**Figure S18.** HRMS spectrum of **5**.

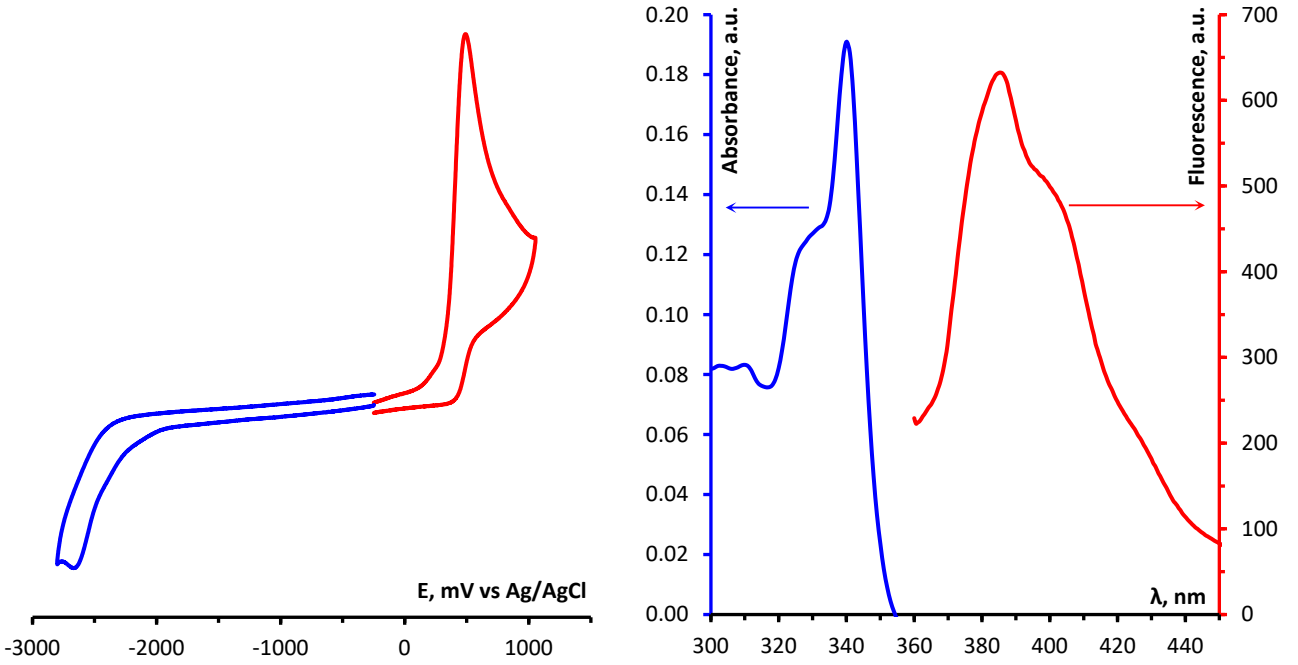


**Figure S19.** (*left*) CV curves of oxidation (*red*) and reduction (*blue*) of **2** (C = 3 mM) in a 0.1 M $Bu_4NBF_4$/DMF supporting electrolyte on a glassy carbon disc electrode at a potential scan rate of 100 mV $s^{-1}$. (*right*) Absorbance and fluorescence spectra of **2** in DMF (C = 0.1 mM).

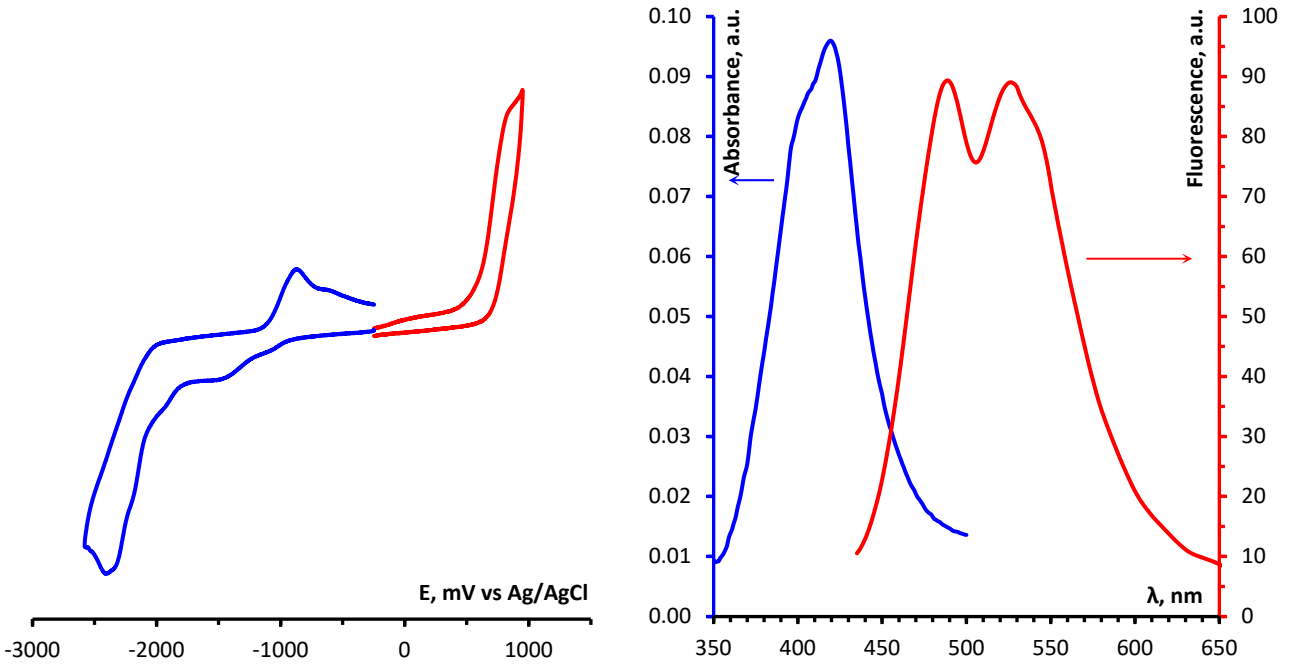


**Figure S20.** (*left*) CV curves of oxidation (*red*) and reduction (*blue*) of **3** (C = 3 mM) in a 0.1 M $Bu_4NBF_4$/DMF supporting electrolyte on a glassy carbon disc electrode at a potential scan rate of 100 mV $s^{-1}$. (*right*) Absorbance and fluorescence spectra of **3** in DMF (C = 0.1 mM).

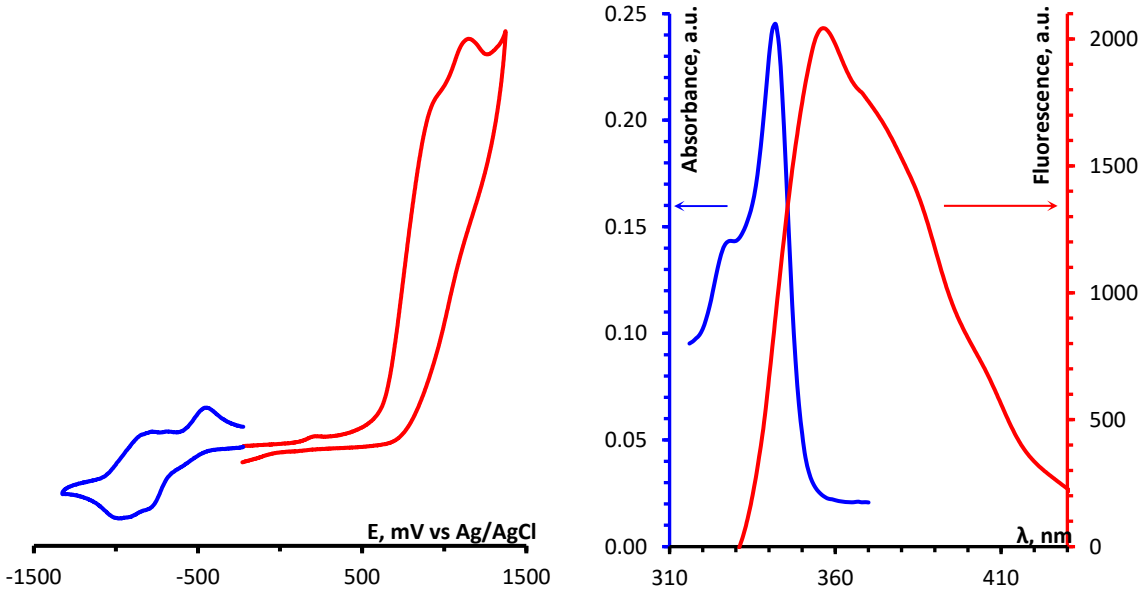


**Figure S21.** (*left*) CV curves of oxidation (*red*) and reduction (*blue*) of **5** (C = 3 mM) in a 0.1 M $Bu_4NBF_4$/DMF supporting electrolyte on a glassy carbon disc electrode at a potential scan rate of 100 mV $s^{-1}$. (*right*) Absorbance and fluorescence spectra of **5** in DMF.

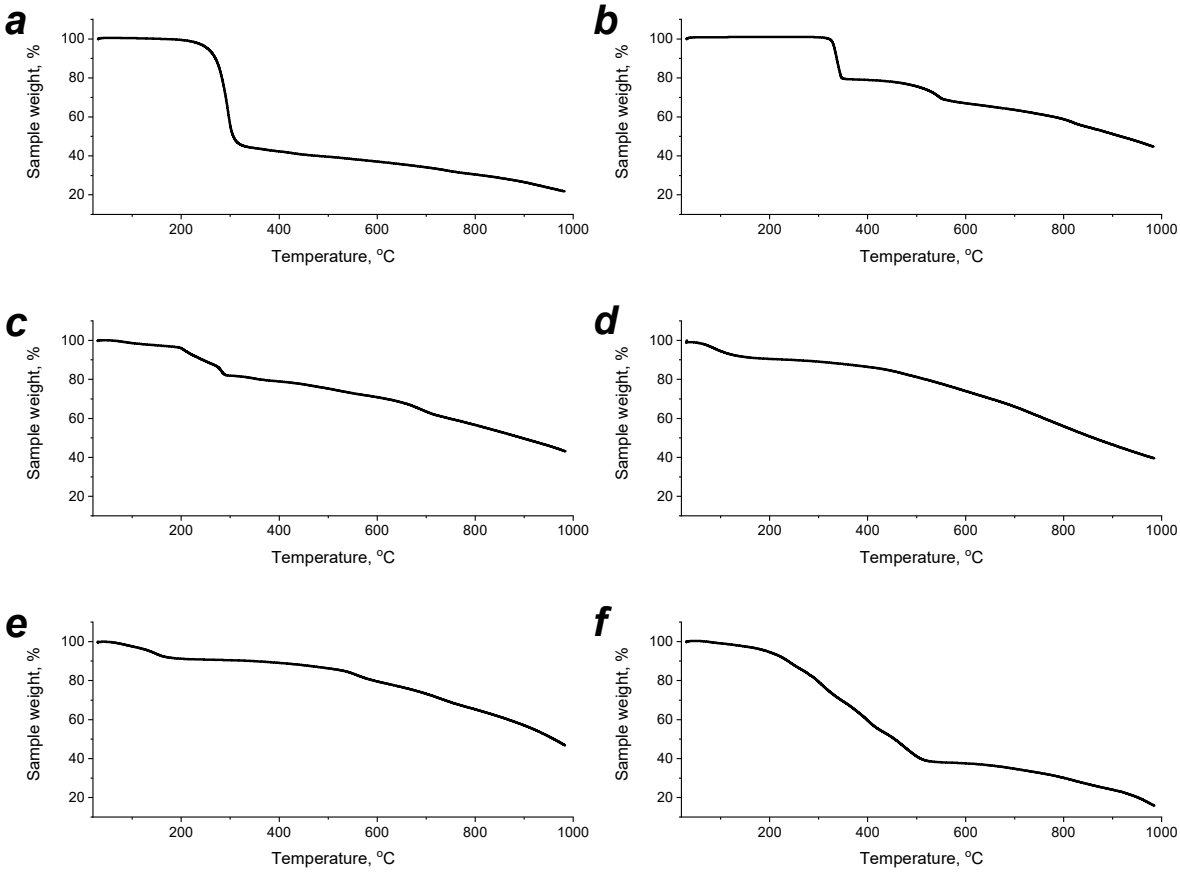


**Figure S22**. Thermal gravimetry profiles of compounds **1** (a), **2** (b), **3** (c), **4** (d), **5** (e) and **6** (f).

**Table S5**. Modification of surface properties of $PC_{61}BM$ by interlayers **1-6**

| **Sample** | **Surface free energy, mN m$^{-1}$** | **Dispersive part, mN m$^{-1}$** | **Polar part, mN m$^{-1}$** | **Average water contact angle, deg.** | **Average $CH_2I_2$ contact angle, deg.** |
|---|---|---|---|---|---|
| $PC_{61}BM$/**1** | 54.6±1.4 | 48.3±0.7 | 6.3±0.7 | 67.4±1.8 | 18.1±2.5 |
| $PC_{61}BM$/**2** | 49.2±2.1 | 47.1±1.8 | 2.1±0.4 | 80.6±1.1 | 22.1±2.5 |
| $PC_{61}BM$/**3** | 51.7±1.0 | 46.9±0.4 | 4.8±0.6 | 71.9±1.5 | 22.9±1.2 |
| $PC_{61}BM$/**4** | 50.4±0.7 | 46.4±0.2 | 4.0±0.5 | 74.6±1.3 | 24.4±0.6 |
| $PC_{61}BM$/**5** | 68.3±2.0 | 47.7±0.5 | 21.0±1.5 | 38.2±2.9 | 20.2±1.7 |
| $PC_{61}BM$/**6** | 52.8±1.6 | 47.7±1.1 | 5.2±0.6 | 70.6±1.4 | 20.4±3.5 |
| $PC_{61}BM$ | 48.0±0.8 | 47.7±0.7 | 0.2±0.1 | 91.1±1.1 | 20.2±2.2 |

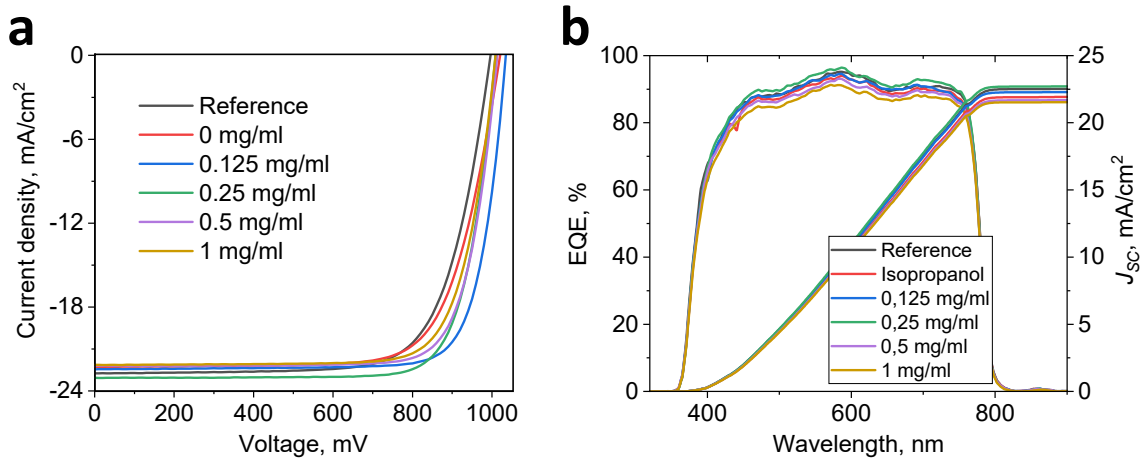


**Figure S23**. *J-V* curves (a) and EQE spectra (b) of perovskite solar cells with different concentrations of compound **1**

**Table S6**. Photovoltaic parameters of perovskite solar cells using compound **1** as interlayer*

| Concentration of **1**, mg/ml | $V_{OC}$, mV | $J_{SC}$, mA/cm$^2$ | FF, % | PCE, % |
|---|---|---|---|---|
| Reference | 1003±18 (996) | 22.3±0.5 (22.7) | 72±3 (73) | 15.5±1.0 (16.5) |
| 0 | 999±21 (1020) | 22.5±0.4 (22.1) | 75±2 (74) | 16.0±0.7 (16.7) |
| 0.125 | 1019±28 (1035) | 22.5±0.5 (22.5) | 76±4 (80) | 17.6±1.0 (18.6) |
| 0.25 | 1002±19 (1009) | 22.5±0.6 (23.0) | 79±1 (79) | 18.0±0.3 (18.3) |
| 0.5 | 1014±11 (1014) | 20.6±0.3 (22.2) | 78±2 (79) | 17.0±0.8 (17.8) |
| 1 | 998±20 (1008) | 21.3±0.8 (22.0) | 76±3 (78) | 17.0±0.3 (17.3) |

* - Average parameters for a batch of 16 cells are given, while the champion cell characteristics are presented in brackets.

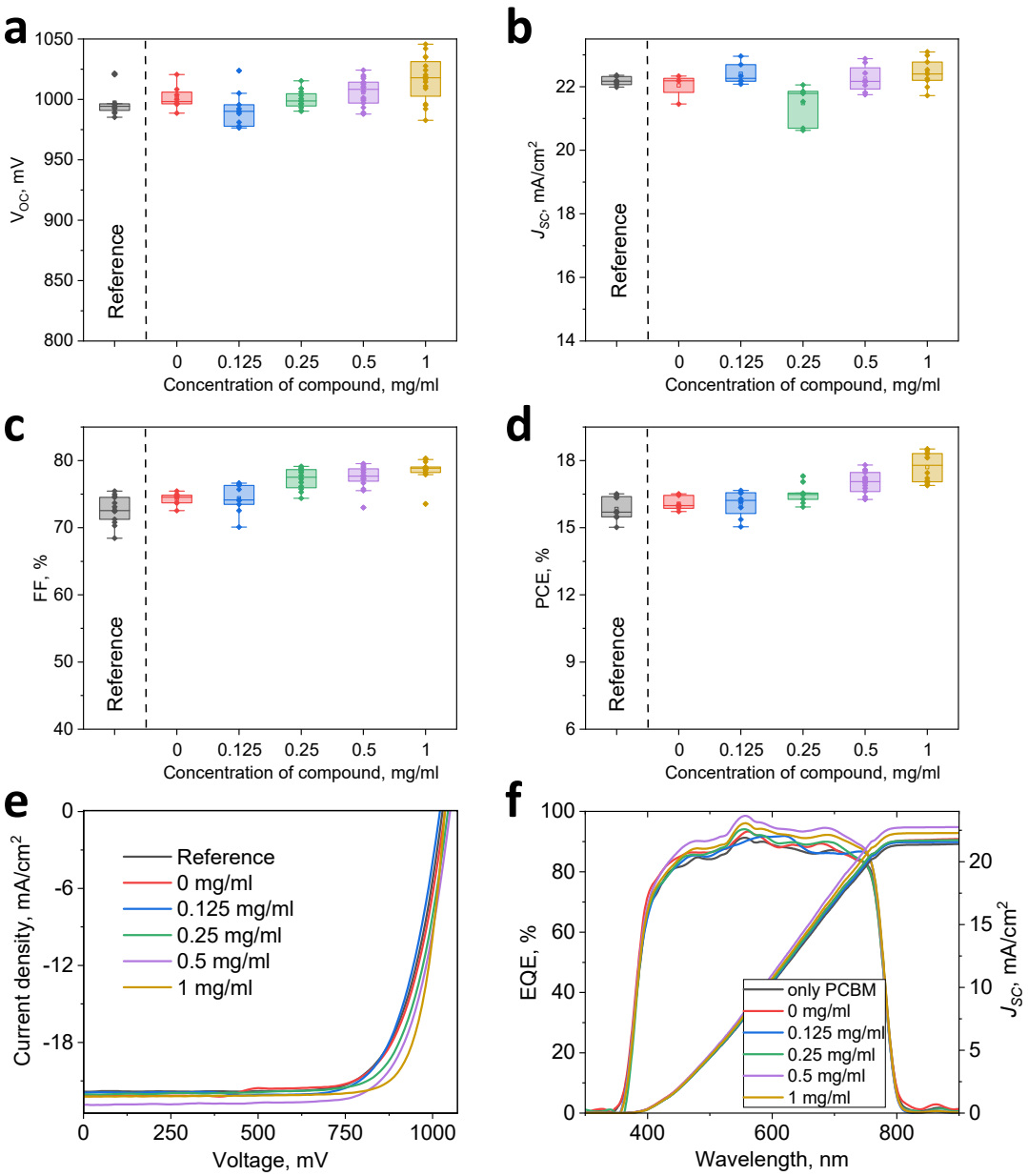


**Figure S24**. $V_{OC}$ (a), $J_{SC}$ (b), FF (c) and PCE (d) of PSCs as a function of concentration of **2**. *J*-V curves (e) and EQE (f) of the best devices

**Table S7**. Photovoltaic parameters of best solar cells with using of **2** as interlayer

| Concentration of **2**, mg/ml | $V_{OC}$, mV | $J_{SC}$, mA/cm$^2$ | FF, % | PCE, % |
|---|---|---|---|---|
| Reference | 1002±29 (1027) | 22.0±0.4 (21.7) | 73±3 (74) | 16.0±0.5 (16.5) |
| 0 | 997±11 (1035) | 21.3±1.0 (22.2) | 73±1 (72) | 16.3±0.3 (16.5) |
| 0.125 | 985±10 (1021) | 22.2±0.8 (22.0) | 74±3 (74) | 16.2±0.5 (16.6) |
| 0.25 | 1007±9 (1044) | 21.5±0.6 (22.1) | 77±2 (75) | 16.7±0.6 (17.3) |
| 0.5 | 1037±17 (1050) | 22.4±0.5 (22.9) | 77±3 (74) | 17.5±0.4 (17.8) |
| 1 | 1033±12 (1040) | 22.5±0.5 (22.2) | 77±1 (80) | 17.9±0.6 (18.5) |

* - Average parameters for a batch of 16 cells are given, while the champion cell characteristics are presented in brackets.

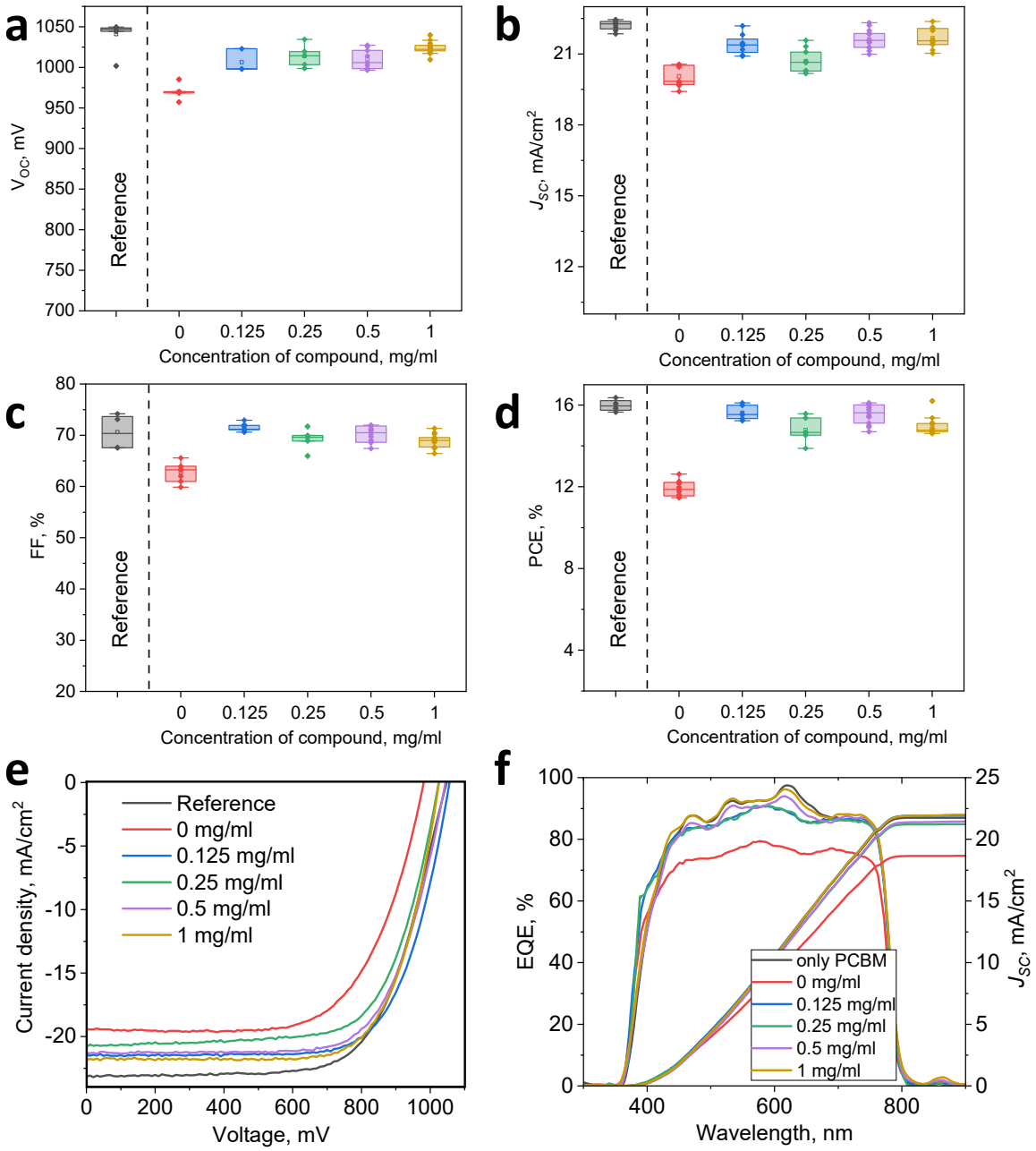


**Figure S25**. $V_{OC}$ (a), $J_{SC}$ (b), FF (c) and PCE (d) of PSCs as a function of concentration of **3**, *J*-V curves (e) and EQE (f) of the best devices

**Table S8**. Photovoltaic parameters of best solar cells with using of **3** as interlayer

| Concentration of **3**, mg/ml | $V_{OC}$, mV | $J_{SC}$, mA/cm$^2$ | FF, % | PCE, % |
|---|---|---|---|---|
| Reference | 1034±17 (1045) | 22.6±0.5 (23.1) | 70±3 (68) | 15.8±0.6 (16.4) |
| 0 | 973±12 (981) | 20.0±0.6 (19.4) | 66±2 (66) | 12.1±0.5 (12.6) |
| 0.125 | 993±10 (1056) | 21.9±0.3 (21.5) | 71±2 (71) | 15.5±0.6 (16.1) |
| 0.25 | 1032±12 (1044) | 21.0±0.6 (21.3) | 69±3 (70) | 15.0±0.6 (15.6) |
| 0.5 | 1013±14 (1024) | 22.0±0.3 (21.9) | 69±3 (72) | 15.8±0.3 (16.1) |
| 1 | 1023±16 (1022) | 22.0±0.3 (21.5) | 72±2 (74) | 15.8±0.5 (16.3) |

* - Average parameters for a batch of 16 cells are given, while the champion cell characteristics are presented in brackets.

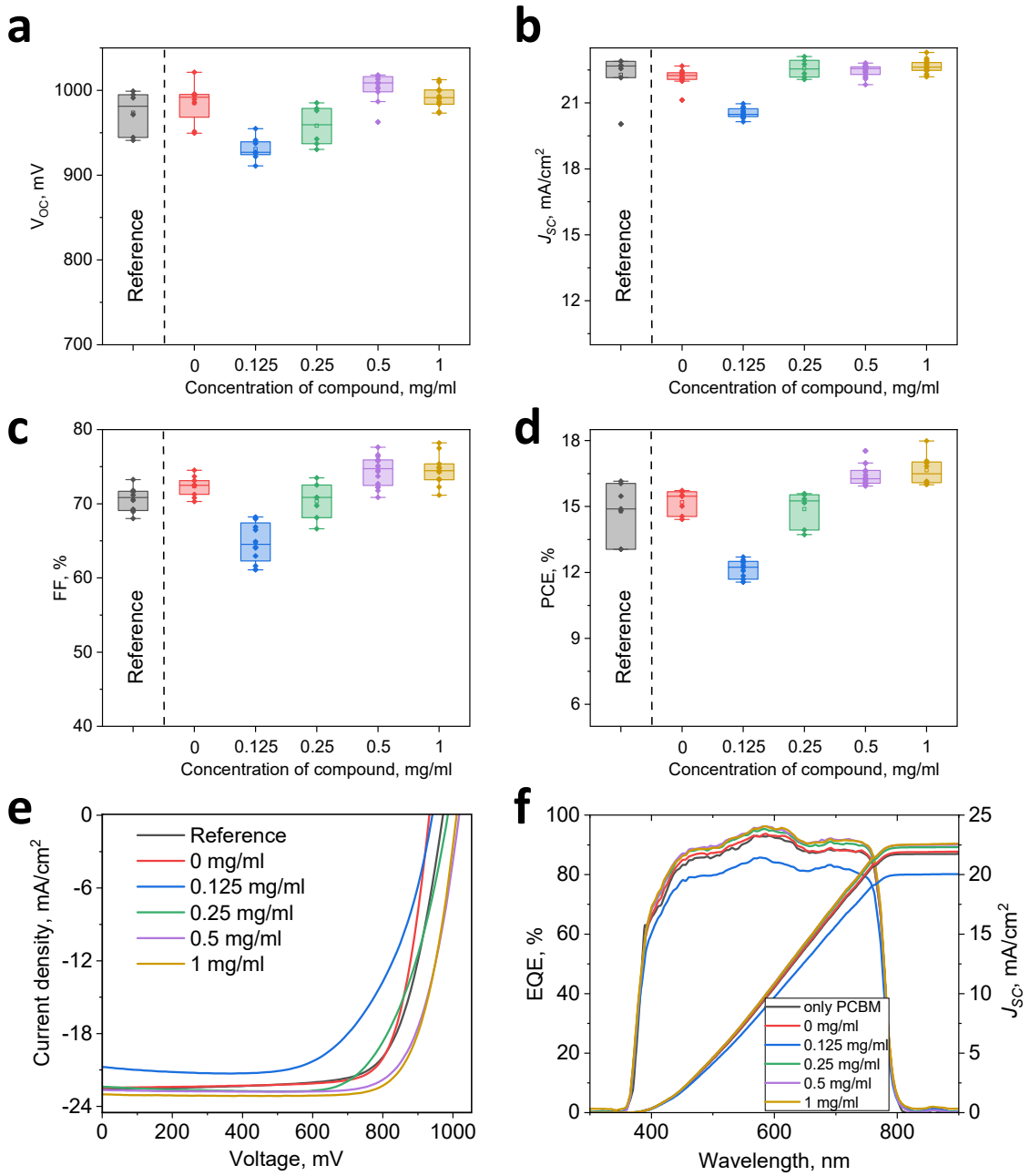


**Figure S26**. $V_{OC}$ (a), $J_{SC}$ (b), FF (c) and PCE (d) of PSCs as a function of concentration of **4**, *J*-V curves (e) and EQE (f) of the best devices

**Table S9**. Photovoltaic parameters of best solar cells with using of **4** as interlayer

| Concentration of **4**, mg/ml | $V_{OC}$, mV | $J_{SC}$, mA/cm$^2$ | FF, % | PCE, % |
|---|---|---|---|---|
| Reference | 968±31 (972) | 22.3±0.6 (22.7) | 70±3 (73) | 14.1±2.0 (16.1) |
| 0 | 969±43 (930) | 22.2±0.5 (22.3) | 73±5 (78) | 14.8±0.9 (16.2) |
| 0.125 | 920±35 (941) | 20.4±0.6 (20.8) | 64±4 (65) | 12.0±0.7 (12.7) |
| 0.25 | 948±37 (985) | 22.4±0.7 (22.3) | 69±5 (71) | 14.2±1.4 (15.6) |
| 0.5 | 982±36 (1017) | 22.5±0.3 (22.7) | 74±4 (76) | 16.1±1.5 (17.5) |
| 1 | 999±23 (1015) | 22.6±0.7 (23.0) | 73±5 (77) | 16.2±1.8 (18.0) |

* - Average parameters for a batch of 16 cells are given, while the champion cell characteristics are presented in brackets.

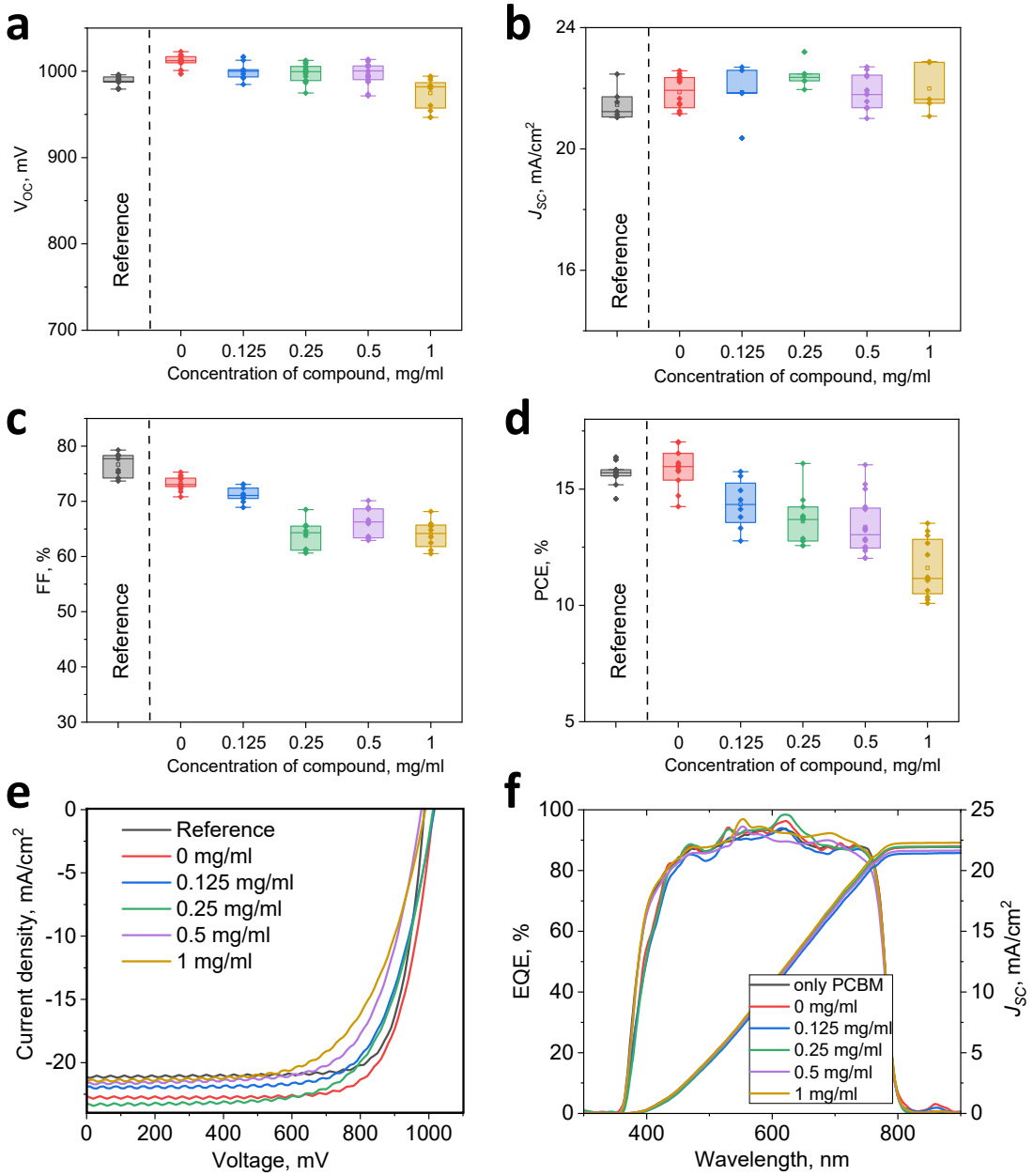


**Figure S27**. $V_{OC}$ (a), $J_{SC}$ (b), FF (c) and PCE (d) of PSCs as a function of concentration of **5**, *J*-V curves (e) and EQE (f) of the best devices

**Table S10**. Photovoltaic parameters of best solar cells with using of **5** as interlayer

| Concentration of **5**, mg/ml | $V_{OC}$, mV | $J_{SC}$, mA/cm$^2$ | FF, % | PCE, % |
|---|---|---|---|---|
| Reference | 988±8 (989) | 21.3±1.2 (21.2) | 76±3 (78) | 15.6±0.8 (16.4) |
| 0 | 1012±11 (1014) | 21.9±0.8 (22.7) | 73±2 (75) | 16.0±1.3 (17.3) |
| 0.125 | 1004±13 (1016) | 21.9±0.8 (21.8) | 70±3 (71) | 14.6±1.1 (15.7) |
| 0.25 | 998±14 (1011) | 21.9±1.3 (23.1) | 64±5 (69) | 14.6±1.5 (16.1) |
| 0.5 | 1004±10 (978) | 22.0±0.7 (21.6) | 66±4 (69) | 12.6±2.0 (14.6) |
| 1 | 985±10 (989) | 22.3±1.0 (21.4) | 65±3 (64) | 12.1±1.4 (13.5) |

* - Average parameters for a batch of 16 cells are given, while the champion cell characteristics are presented in brackets.

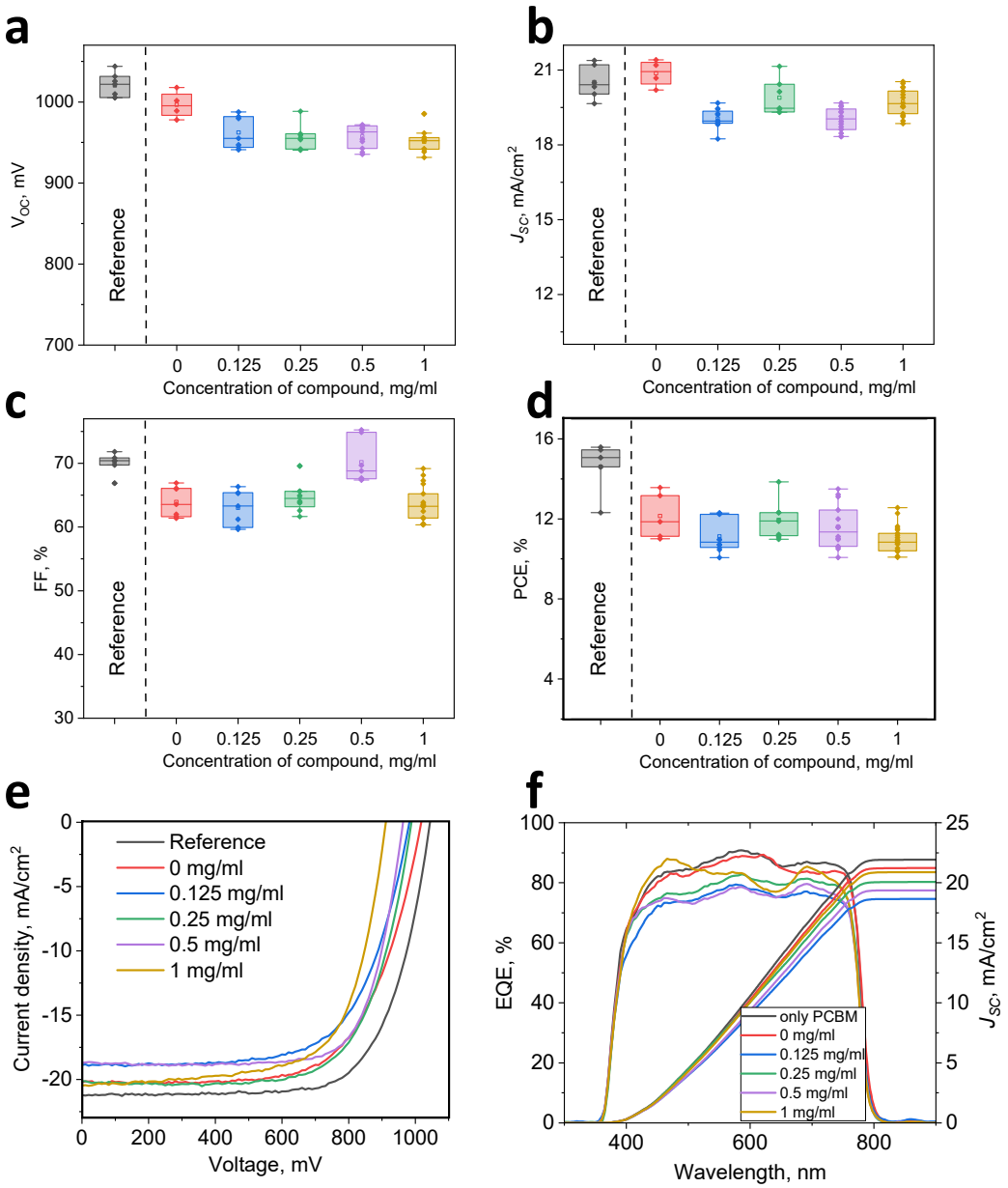


**Figure S28**. $V_{OC}$ (a), $J_{SC}$ (b), FF (c) and PCE (d) of PSCs as a function of concentration of **6**, *J*-V curves (e) and EQE (f) of the best devices

**Table S11**. Photovoltaic parameters of best solar cells with using of **6** as interlayer.

| Concentration of **6**, mg/ml | $V_{OC}$, mV | $J_{SC}$, mA/cm$^2$ | FF, % | PCE, % |
|---|---|---|---|---|
| Reference | 1026±17 (1042) | 20.4±1.0 (21.1) | 69±3 (71) | 13.6±2.0 (15.6) |
| 0 | 1002±16 (1018) | 19.7±1.7 (20.2) | 64±3 (66) | 12.2±1.4 (13.6) |
| 0.125 | 970±18 (980) | 19.0±0.7 (19.3) | 61±4 (65) | 10.7±1.6 (12.3) |
| 0.25 | 972±16 (988) | 20.3±0.9 (20.1) | 66±4 (70) | 12.1±1.7 (13.9) |
| 0.5 | 959±14 (963) | 18.7±1.0 (18.7) | 72±4 (75) | 11.8±1.7 (13.5) |
| 1 | 966±20 (912) | 20.1±1.0 (20.6) | 65±4 (67) | 11.2±1.5 (12.6) |

* - Average parameters for a batch of 16 cells are given, while the champion cell characteristics are presented in brackets.

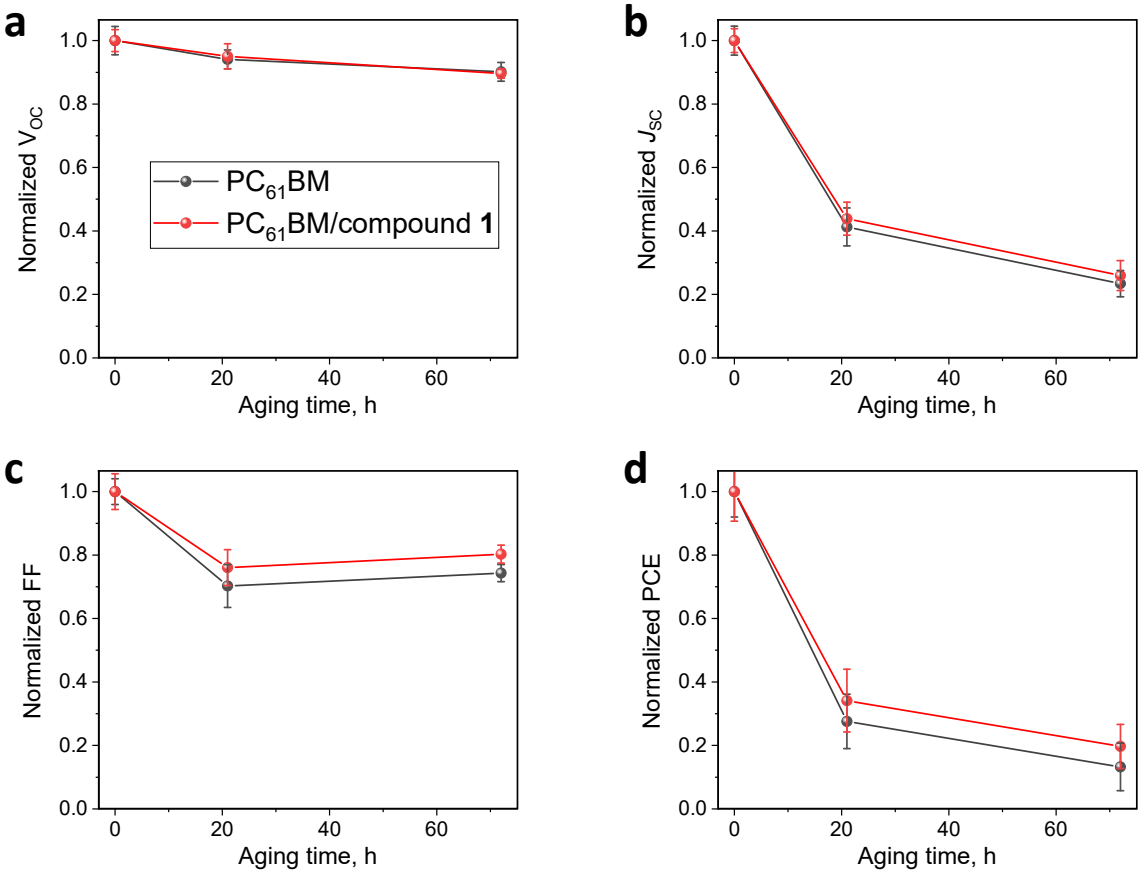


**Figure S29**. The evolution of the normalized open-circuit voltage (a), short-circuit current (b), fill factor (c) and power conversion efficiency (d) of perovskite solar cells using bare $PC_{61}BM$ and its combination with compound 1 as ETL materials.

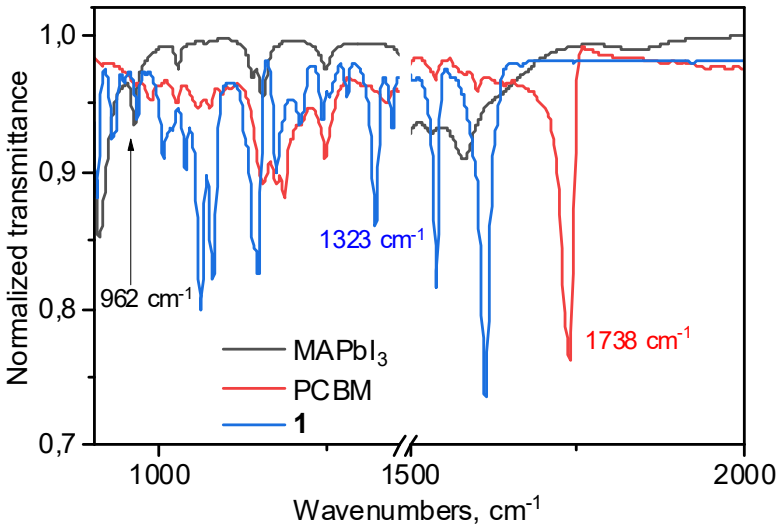


**Figure S30**. ATR FTIR spectra of $MAPbI_3$, $PC_{61}BM$, and **1**.

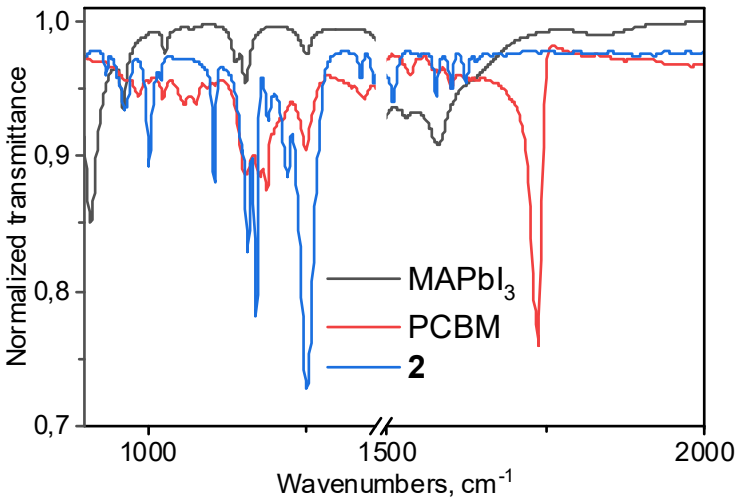


**Figure S31**. ATR FTIR spectra of $MAPbI_3$, $PC_{61}BM$, and **2**.

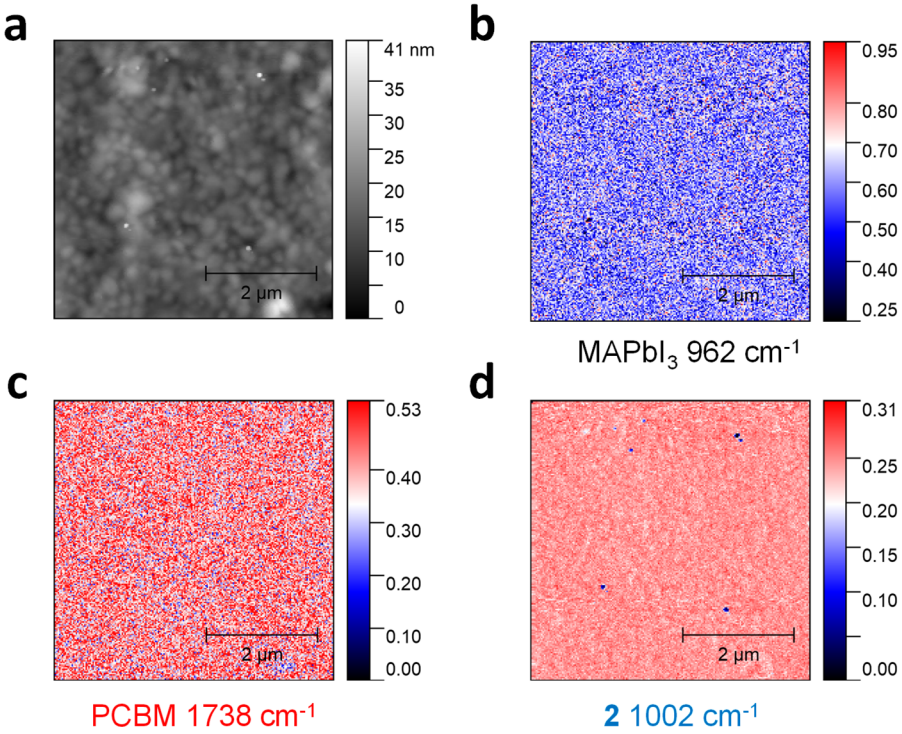


**Figure S32**. AFM topography of ITO/PTA/$MAPbI_3$/$PC_{61}BM$/**2** film (a); mappings of ITO/PTA/$MAPbI_3$/$PC_{61}BM$/**2** topography at frequencies of 962 $cm^{-1}$ (b), 1738 $cm^{-1}$ (c), and 1002 $cm^{-1}$ (d), which are characteristic for $MAPbI_3$, $PC_{61}BM$, and **2**, respectively.

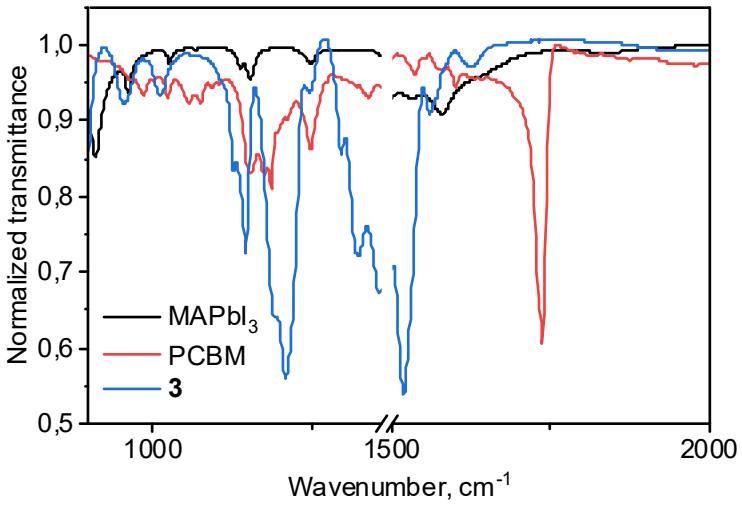


**Figure S33**. ATR FTIR spectra of $MAPbI_3$, $PC_{61}BM$, and **3**.

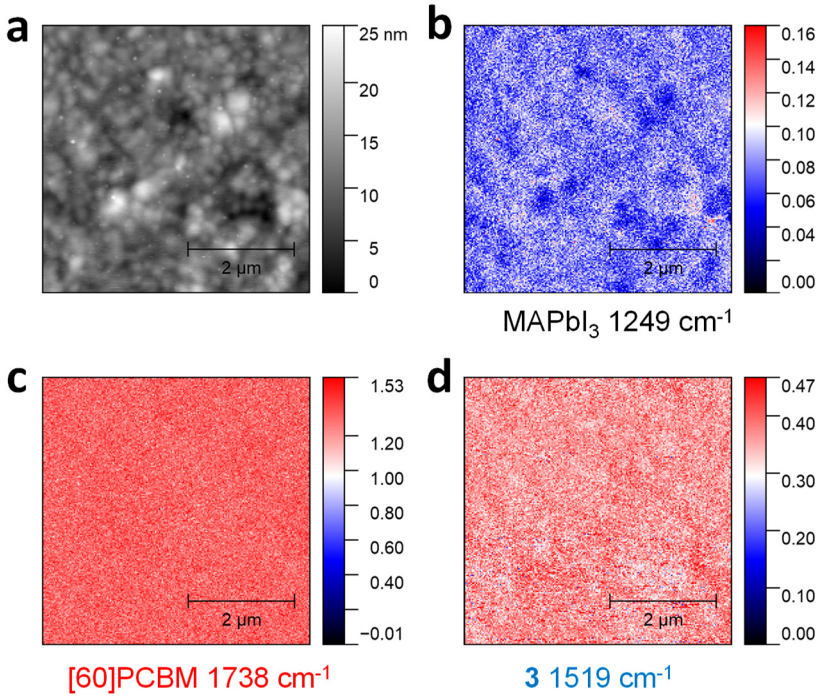


**Figure S34**. AFM topography of ITO/PTA/$MAPbI_3$/$PC_{61}BM$/**3** film (a); mappings of ITO/PTA/$MAPbI_3$/$PC_{61}BM$/**3** topography at frequencies of 1249 $cm^{-1}$ (b), 1738 $cm^{-1}$ (c), and 1519 $cm^{-1}$ (d), which are characteristic for $MAPbI_3$, $PC_{61}BM$, and **3**, respectively.

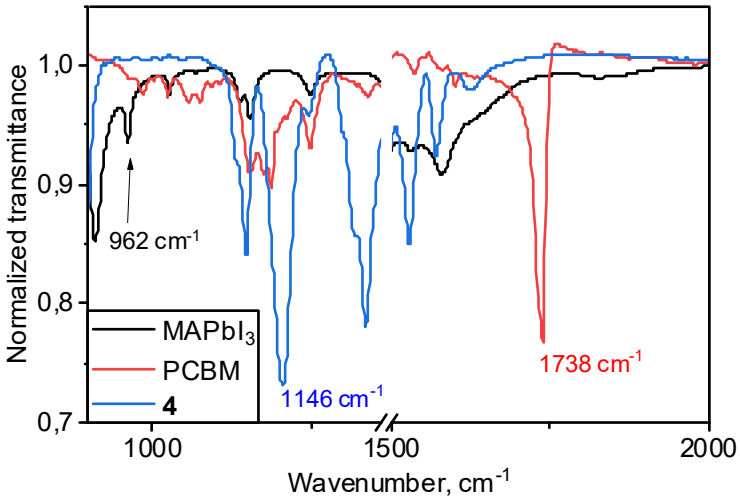


**Figure S35**. ATR FTIR spectra of $MAPbI_3$, $PC_{61}BM$, and **4**.

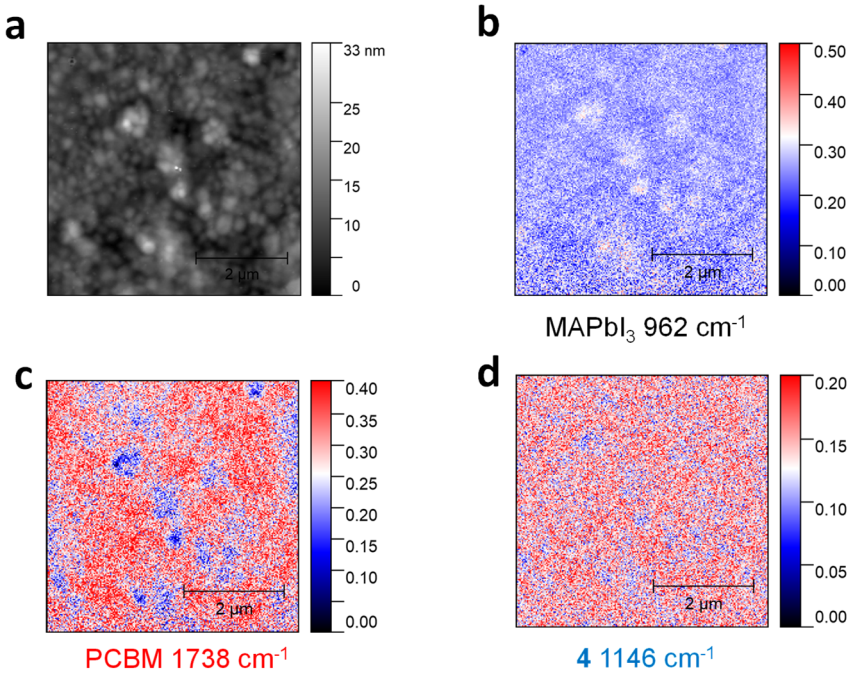


**Figure S36**. AFM topography of ITO/PTA/$MAPbI_3$/$PC_{61}BM$/**4** film (a); mappings of ITO/PTA/$MAPbI_3$/$PC_{61}BM$/**4** topography at frequencies of 962 $cm^{-1}$ (b), 1738 $cm^{-1}$ (c), and 1146 $cm^{-1}$ (d), which are characteristic for **4**, $PC_{61}BM$, and $MAPbI_3$, respectively.

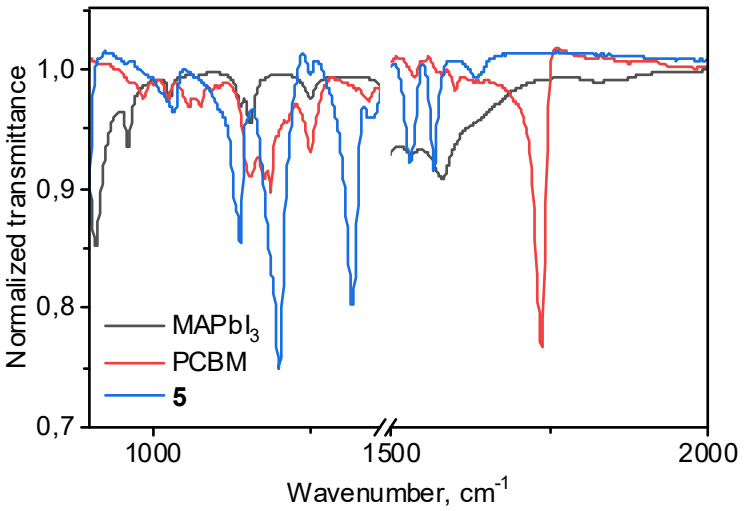


**Figure S37**. ATR FTIR spectra of $MAPbI_3$, $PC_{61}BM$, and **5**.

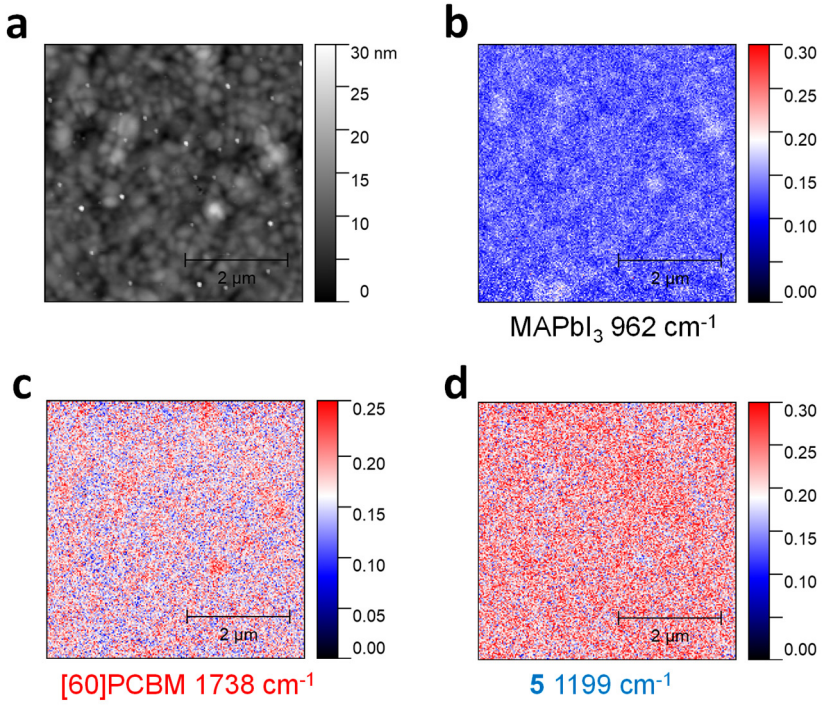


**Figure S38**. AFM topography of ITO/PTA/$MAPbI_3$/$PC_{61}BM$/**5** film (a); mappings of ITO/PTA/$MAPbI_3$/$PC_{61}BM$/**5** topography at frequencies of 962 $cm^{-1}$ (b), 1738 $cm^{-1}$ (c), and 1199 $cm^{-1}$ (d), which are characteristic for **5**, $PC_{61}BM$, and $MAPbI_3$, respectively.

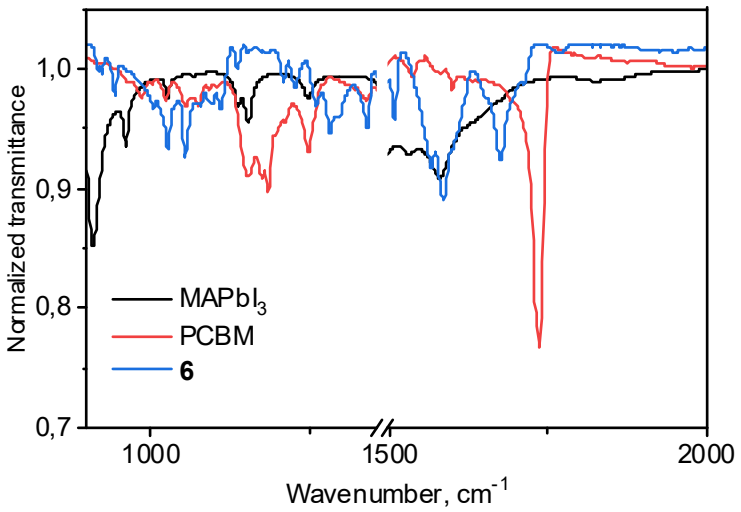


**Figure S39**. ATR FTIR spectra of $MAPbI_3$, $PC_{61}BM$, and **6**.

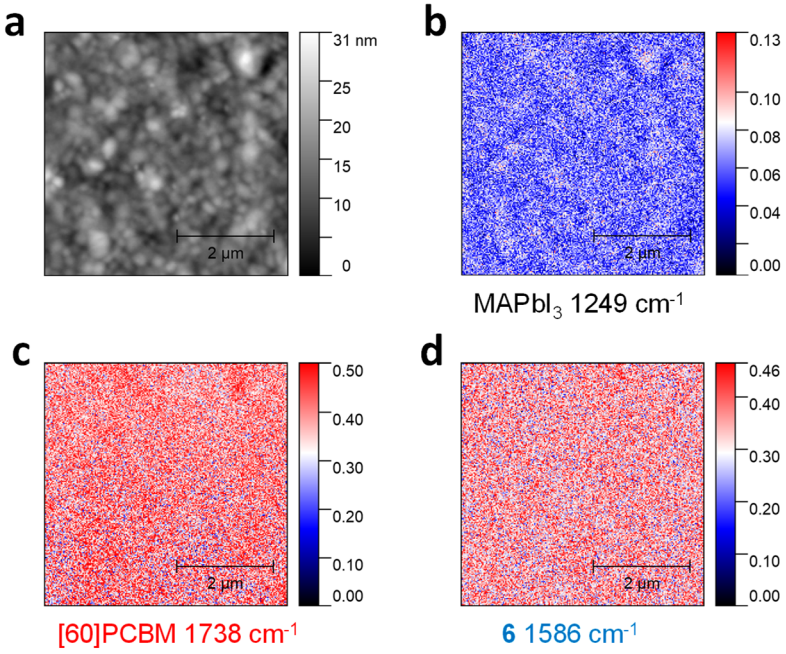


**Figure S40**. AFM topography of ITO/PTA/$MAPbI_3$/$PC_{61}BM$/**6** film (a); mappings of ITO/PTA/$MAPbI_3$/$PC_{61}BM$/**6** topography at frequencies of 962 $cm^{-1}$ (b), 1738 $cm^{-1}$ (c), and 1586 $cm^{-1}$ (d), which are characteristic for **6**, $PC_{61}BM$, and $MAPbI_3$, respectively.